# Shape of the Capillary Meniscus around an Electrically Charged Particle at a Fluid Interface: Comparison of Theory and Experiment

Krassimir D. Danov, Peter A. Kralchevsky,* and Mariana P. Boneva

*Laboratory of Chemical Physics & Engineering, Faculty of Chemistry, University of Sofia, 1164 Sofia, Bulgaria*

*Received October 12, 2005. In Final Form: January 9, 2006*

Here, we consider in detail the problem of the shape of the capillary meniscus around a charged colloidal particle, which is attached to a fluid interface: oil/water or air/water. The meniscus profile is influenced by the electric field created by charges at the particle/nonpolar fluid boundary. We digitized the coordinates of points from the meniscus around silanized glass spheres (200−300 $\mu$m in radius) attached to the tetradecane/water interface. The theoretical meniscus shape is computed in three different ways that give numerically coincident results. It is proven that for sufficiently small particles the meniscus profile can be expressed as a superposition of pure electric and gravitational deformations. Special attention is paid to the comparison of theory and experiment. A procedure for data processing is developed that allows one to obtain accurate values of the contact angle and surface charge density from the fit of the experimental meniscus profile. For all investigated particles, excellent agreement between theory and experiment is achieved. The results indicate that the electric field gives rise to an interfacial deformation of medium range and considerable amplitude.

## 1. Introduction

Monolayers of colloidal particles at a fluid interface (oil/water or air/water) are widely studied in relation to the properties of Pickering emulsions,[1,2] the formation of particle arrays and colloidosomes at the surface of emulsion drops,[3,4] and the attainment of colloidal structures with various applications.[5−8] The experiments with such systems indicate that the adsorbed particles interact via repulsive and attractive forces, whose range and magnitude are often much greater than for the DLVO surface forces.[9−20] When the *attractive* forces prevail, one observes particle aggregation and the formation of large-scale densely packed colloidal structures (mesostructures).[11−19] In particular, an indication of the action of a long-range attractive force has been found for particles at the surface of an emulsion drop.[20]

When the *repulsive* forces are significant, the particles form hexagonal arrays of intersite distance considerably greater than the particle diameter.[9,20−28] The analysis of the experimental results shows that these repulsive forces have an electrostatic origin. In some cases, the addition of electrolyte to the aqueous phase suppresses the repulsion,[14,20] whereas in other cases the electrolyte does not affect the long-range repulsion, even at high ionic strengths.[21−23] The latter finding has been explained by the presence of electric charges at the particle/oil[21−23,27] and particle/air[28] interfaces. Because the electric field is not screened in the nonpolar phase (oil, air), the adsorbed particles experience a long-range Coulombic repulsion. It is interesting that this repulsive force depends on the particle protrusion in the nonpolar phase (i.e., on the contact angle). Horozov et al.[23,26−28] experimentally established that very hydrophobic particles with large contact angles form well-ordered monolayers at interparticle distances larger than 3 particle diameters. In contrast, the monolayers of less hydrophobic particles (with contact angles smaller than 115°) were disordered and aggregated. The disorder−order transition in the monolayer structure occurred in the interval of contact angles between 115 and 129°. (Here and hereafter, we follow the standard convention that the contact angle is measured across the water phase.)

One of the possible explanations of the observed interparticle attraction is the action of lateral capillary forces, which are due

* Corresponding author. E-mail: pk@lcpe.uni-sofia.bg. Phone: (+359) 2-962 5310. Fax: (+359) 2-962 5438.

(1) Binks, B. P. *Curr. Opin. Colloid Interface Sci.* **2002**, *7*, 21−41.
(2) Aveyard, R.; Binks, B. P.; Clint, J. H. *Adv. Colloid Interface Sci.* **2003**, *100−102*, 503−546.
(3) Velev, O. D.; Furusawa, K.; Nagayama, K. *Langmuir* **1996**, *12*, 2374−2384.
(4) Dinsmore, A. D.; Hsu, M. F.; Nikolaides, M. G.; Marquez, M.; Bausch, A. R.; Weitz, D. A. *Science* **2002**, *298*, 1006−1009.
(5) Kralchevsky, P. A.; Denkov, N. D. *Curr. Opin. Colloid Interface Sci.* **2001**, *6*, 383−401.
(6) Kralchevsky, P. A.; Nagayama, K. *Particles at Fluid Interfaces and Membranes*; Elsevier: Amsterdam, 2001.
(7) Fan, F.; Stebe, K. J. *Langmuir* **2004**, *20*, 3062−3067.
(8) Abkarian, M.; Nunes, J.; Stone, H. A. *J. Am. Chem. Soc.* **2004**, *126*, 5978−5979.
(9) Pieranski, P. *Phys. Rev. Lett.* **1980**, *45*, 569−572.
(10) Levine, S.; Bowen, B. D.; Partridge, S. J. *Colloids Surf.* **1989**, *38*, 325−343.
(11) Hurd, A. J.; Schaefer, D. W. *Phys. Rev. Lett.* **1985**, *54*, 1043−1046.
(12) Onoda, G. Y. *Phys. Rev. Lett.* **1985**, 55, 226−229.
(13) Armstrong, A. J.; Mockler, R. C.; O'Sullivan, W. J. *J. Phys.: Condens. Matter* **1989**, *1*, 1707−1730.
(14) Robinson, D. J.; Earnshaw, J. *Phys. Rev. A* **1992**, *46*, 2045−2054.
(15) Ghezzi, F.; Earnshaw, J. C. *J. Phys.: Condens. Matter* **1997**, *9*, L517−L523.
(16) Ruiz-Garcia, J.; Gámez-Corrales, R.; Ivlev, B. I. *Physica A* **1997**, *236*, 97−104.
(17) Ruiz-Garcia, J.; Gámez-Corrales, R.; Ivlev, B. I. *Phys. Rev. E* **1998**, *58*, 660−663.
(18) Stamou, D.; Duschl, C.; Johannsmann, D. *Phys. Rev. E*, **2000**, *62*, 5263−5272.
(19) Fernández-Toledano, J. C.; Moncho-Jordá, A.; Martínez-López, F.; Hidalgo-Álvarez, R. *Langmuir* **2004,** *20*, 6977−6980.
(20) Nikolaides, M. G.; Bausch, A. R.; Hsu, M. F.; Dinsmore, A. D.; Brenner, M. P.; Gay, C.; Weitz, D. A. *Nature* **2002**, *420*, 299−301.
(21) Aveyard, R.; Clint, J. H.; Nees, D.; Paunov, V. N. *Langmuir* **2000**, *16*, 1969−1979.
(22) Aveyard, R.; Binks, B. P.; Clint, J. H.; Fletcher, P. D. I.; Horozov, T. S.; Neumann, B.; Paunov, V. N.; Annesley, J.; Botchway, S. W.; Nees, D.; Parker, A. W.; Ward, A. D.; Burgess, A. N. *Phys. Rev. Lett.* **2002**, *88*, 246102.
(23) Horozov, T. S.; Aveyard, R.; Clint, J. H.; Binks, B. P. *Langmuir* **2003**, *19*, 2822−2829.
(24) Stancik E. J.; Kouhkan, M.; Fuller, G. G. *Langmuir* **2004**, *20*, 90−94.
(25) Stancik E. J.; Fuller, G. G. *Langmuir* **2004**, *20*, 4805−4808.
(26) Horozov, T. S.; Aveyard, R.; Clint, J. H. *Langmuir* **2005**, *21*, 2330−2341.
(27) Horozov, T. S.; Aveyard, R.; Binks, B. P.; Clint, J. H. *Langmuir* **2005**, *21*, 7407−7412.
(28) Horozov, T. S.; Binks, B. P. *Colloids Surf., A* **2005**, *267*, 64−73.

10.1021/la052749z CCC: $33.50 
Published on Web 02/07/2006

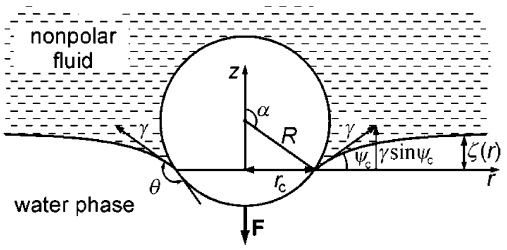


**Figure 1.** Sketch of a particle at the interface between water and a nonpolar fluid (oil, air). $\gamma$ is the interfacial tension; $R$ and $r_c$ are the radii of the particle and the three-phase contact line; $\alpha$ and $\theta$ are the central angle and contact angle; $\psi_c$ is the meniscus slope angle at the contact line; and **F** is a normal force acting on the particle, which can be of electric and/or gravitational origin.

to the overlap of the menisci around the separate particles.[20,29−32] The meniscus shape, $z = \zeta(r)$, around an isolated particle on a horizontal fluid interface (Figure 1) represents a solution of the Laplace equation of capillarity, which can be linearized for the case of small slope, $(d\zeta/dr)^2 \ll 1$:[29,31,32]

$$\frac{1}{r}\frac{d}{dr}\left(r\frac{d\zeta}{dr}\right) - q^2\zeta = 0 \qquad (1.1)$$

where $q^2 = \Delta\rho g/\gamma$; $\Delta\rho$ is the difference between the mass densities of the lower and upper fluid phases, $\gamma$ is the interfacial tension, and $g$ is the acceleration due to gravity. The normal force, $F$, acting on the particle must be counterbalanced by the vertical resultant of the interfacial-tension force acting at the contact line on the particle surface

$$F = 2\pi r_c \gamma \sin\psi_c \qquad (1.2)$$

where $\psi_c$ is the meniscus slope angle at the contact line, which is a circumference of radius $r_c$ (Figure 1). For small meniscus slope, we have $\sin\psi_c \approx \tan\psi_c = {}^{d\zeta}/_{dr}$ at $r = r_c$, and then eq 1.2 gives

$$\frac{d\zeta}{dr}\Big|_{r=r_c} = \frac{F}{2\pi r_c \gamma} \qquad (1.3)$$

The solution of eq 1.1, along with the boundary condition of eq 1.3, reads[20,31,32]

$$\zeta(r) = \frac{-FK_0(qr)}{2\pi\gamma q r_c K_1(qr_c)} \approx \frac{F}{2\pi\gamma}\ln\left(\frac{r}{r_0}\right) \qquad (1.4)$$

where $r_0$ is a constant and $K_0$ and $K_1$ are modified Bessel functions of zeroth and first order.[33−35] In the last step, we have used the asymptotic expansions of $K_0$ and $K_1$ for $qr \ll 1$ (for particle radius much smaller than the capillary length, $q^{-1}$)[33−35]

$$K_0(x) \approx -\ln\left(\frac{\gamma_e x}{2}\right) \qquad K_1(x) \approx \frac{1}{x} \qquad \text{for } x^2 \ll 1 \qquad (1.5)$$

where $\gamma_e$ is the Euler−Masceroni constant ($\gamma_e = 1.781072418...$).

Note, that despite the logarithmic behavior of $K_0(qr)$ at short distances (eq 1.5) this function and the meniscus profile $\zeta(r)$ decay exponentially at long distances.

Nikolaides et al.[20] noted that the electric field generated by the particles creates an electrostatic contribution to the pressure, $p_{el}$, which vanishes as $1/r^6$. Megens and Aizenberg[36] included the effect of $p_{el}$ in the Laplace equation:

$$\frac{1}{r}\frac{d}{dr}\left(r\frac{d\zeta}{dr}\right) - q^2\zeta = \frac{1}{\gamma}p_{el}(r) \qquad (1.6)$$

See eq 1.1 above. Then, if we (approximately) substitute $p_{el} = A/r^6$ into eq 1.6 ($A$ = const.) and neglect the gravitational term, $q^2\zeta$, the result reads[36]

$$\zeta(r) = -\frac{F}{8\pi\gamma}\left(\frac{r_c}{r}\right)^4 \qquad (1.7)$$

where the boundary condition, eq 1.3, has been used to determine $A$. For experimental parameter values, eq 1.7 predicts a faster decay of the meniscus than eq 1.4.

In a recent study,[37] we carried out experiments with larger particles (of radius 200−300 $\mu$m), which form microscopically visible menisci (dimples) at the oil/water and air/water interfaces. The side-view photographs showed that the experimental slope angle $\psi_c$ (Figure 1) is much greater (about 15 times) than the "gravitational" value of $\psi_c$, which is the theoretical value calculated under the assumption that only the particle weight and buoyancy force are acting on the particle. The difference between the experimental and gravitational $\psi_c$ was attributed to the action of a normal electric (electrodipping) force, $F^{(el)}$. Thus, the total force exerted at the particle is

$$F = F^{(el)} + F^{(g)} \qquad (1.8)$$

where $F^{(g)}$ is the gravitational force. Moreover, the experiments showed that $F^{(el)}$ is independent of the electrolyte concentration in the aqueous phase, which means that in our case $F^{(el)}$ is dominated by electric charges at the particle/nonpolar fluid boundary rather than at the particle/water boundary.[37] From the experimentally determined $F^{(el)}$, we calculated the surface charge density at the particle/nonpolar fluid boundary, $\sigma_{pn}$, which compares well with results obtained by other authors.[23,26−28] In general, the electrodipping force is a sum of contributions from electric charges at the particle/nonpolar fluid and particle/water interfaces:

$$F^{(el)} = F^{(n)} + F^{(w)} \qquad (1.9)$$

$F^{(n)}$ and $F^{(w)}$ point in the same direction: both of them are pushing the particle into the water phase. Theoretical expressions for calculating $F^{(n)}$ and $F^{(w)}$ have been derived.[37] They are based on modeling the particles as spheres of given surface charge densities instead of point dipoles, as in previous work. An exact numerical solution of the electrostatic boundary problem (in toroidal coordinates) was obtained, which also produces numerical data for the electrostatic pressure, $p_{el}(r)$. Finally, we substituted the calculated $p_{el}(r)$ into the Laplace equation, eq 1.6, and computed a meniscus profile $\zeta(r)$, which was found to agree well with the experimental profile.[37]

In addition to the correct results reported in our previous article,[37] it contains two mistakes that we want to announce and

(29) Nicolson, M. M. *Proc. Cambridge Philos. Soc.* **1949**, *45*, 288−295.
(30) Derjaguin, B. V.; Starov, V. M. *Colloid J. USSR Engl. Transl.* **1977**, *39*, 383−386.
(31) Chan, D. Y. C.; Henry, J. D.; White, L. R. *J. Colloid Interface Sci.* **1981**, *79*, 410−418.
(32) Kralchevsky, P. A.; Nagayama, K. *Adv. Colloid Interface Sci.* **2000**, *85*, 145−192.
(33) Janke, E.; Emde, F.; Lösch, F. *Tables of Higher Functions*; McGraw-Hill: New York, 1960.
(34) Dwight, H. B. *Tables of Integrals and Other Mathematical Data*; Macmillan Co.: New York, 1961.
(35) Abramowitz, M.; Stegun, I. A. *Handbook of Mathematical Functions;* Dover: New York, 1965.
(36) Megens, M.; Aizenberg, J. *Nature* **2003**, *424*, 1014.
(37) Danov, K. D.; Kralchevsky, P. A.; Boneva, M. P. *Langmuir* **2004**, *20*, 6139−6151.

clarify here. First, there is a misprint (noticed by Oettel et al.[38]) in the form of eq 6.2 in ref 37, which is the Laplace equation in toroidal coordinates. The correct form of the latter equation is

$$\frac{x_1^3}{r_c^2}\frac{d}{dx_1}\left(x_1\frac{d\zeta}{dx_1}\right) - q^2\zeta = \frac{1}{\gamma}p_{el} \qquad (1.10)$$

Equation 1.10 can be obtained by substituting $r = r_c/x_1$ into eq 1.6. Equation 6.2 in our article[37] was given only for completeness; it was not used in our calculations, and it had not affected the correctness of the results reported therein. Second, the analysis of eq 1.6 implies that its solution has the following asymptotic behavior at long distances from the particle:

$$\zeta(r) \approx \frac{F^{(g)}}{2\pi\gamma}\ln\left(\frac{r}{r_0}\right) \text{ for } r_c \ll r \ll q^{-1} \qquad (1.11)$$

See ref 39 and section 4.2 below. Note that the logarithmic prefactor in eq 1.11 contains only $F^{(g)}$ and contains no contribution from $F^{(el)}$. As a consequence, our matched asymptotic expansions for the meniscus profile $\zeta(r)$ and interaction energy $U(r)$, eqs 3.25 and 3.26 in ref 37, which are based on eq 1.11 with $F - \lambda F^{(el)}$ instead of $F^{(g)}$, turn out to be incorrect for $r/r_c \geq 4$. In fact, the *short*-range asymptotics of $\zeta(r)$ really contains a logarithmic term with a prefactor proportional to $F - \lambda F^{(el)}$, but this term cannot be matched with the outer asymptotics $BK_0(qr)$ and cannot be used to determine the multiplicative constant $B$. The reason is that the physical problem is characterized by two different length scales (related to the gravity and electric force, scaled by the capillary force); therefore, the conventional matching procedure of Prandtl[40] is inapplicable. The incorrect matching affects only the validity of the results in section 3.7 in ref 37. The rest of ref 37, including the experiment, the theoretical expressions for the electrodipping force ($F^{(w)}$ and $F^{(n)}$), and the numerical solutions, is correct.

The problem of quantifying the meniscus profile, $\zeta(r)$ for $r_c \leq r < \infty$, in the case of an electrically charged particle is the main subject of the present article. Our goal here is to develop a procedure for processing experimental data for $\zeta(r)$, which would allow one to determine the surface charge density, $\sigma_{pn}$, at the particle−nonpolar fluid boundary and to obtain a more accurate value of the contact angle, $\theta$, in comparison with that obtained from the simple goniometric method. This problem is nontrivial because the meniscus shape is affected by the electric field engendered by the particle. In other words, to calculate $\zeta(r)$ we need to know $p_{el}(r)$; see eq 1.6. We restrict our analysis to the case of a *single* particle. Such a study is a prerequisite for a quantitative and reliable analysis of the more complex problem of two attached particles and the electric-field-induced capillary interaction between them. The latter problem has been the subject of controversy in the literature.[36,39,41,42]

In the following, we will assume that the particle is spherical and the fluid interface is planar before particle attachment. Another assumption, which is fulfilled for most systems of experimental interest, is that the particles are sufficiently small, $(qr_c)^2 \ll 1$, and that the slope of the interfacial deformation produced by them is also small, $(d\zeta/dr)^2 \ll 1$. In addition, we will restrict our considerations to the case when the electric effects are dominated by charges located at the boundary of the particle with the nonpolar fluid (oil, air). This case corresponds to a situation that has been observed in many experiments.[21−23,26−28,37] In other words, we presume that

$$F^{(n)} \gg F^{(w)} \text{ and } F^{(el)} \approx F^{(n)} \qquad (1.12)$$

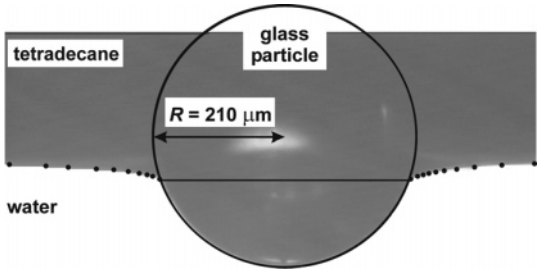


**Figure 2.** Side-view photograph of a silanized glass particle at the water−tetradecane interface. The coordinates of selected points (denoted in the figure) on the left- and right-hand-side meniscus profiles have been digitized and compared with the theoretical profile (Figure 3 and section 7.4).

The article is organized as follows. In section 2, we describe the experiment and the procedure for data acquisition. In section 3, we consider three different methods for calculating the theoretical meniscus profile. Section 4 is devoted to the range of the electric-field-induced interfacial deformation and to the asymptotics of the meniscus profile at long distances from the particle. In section 5, we prove that for sufficiently small particles the interfacial shape can be expressed as a superposition of electric and gravitational deformations. The magnitudes of the latter two types of deformations are compared in section 6 for different particle radii and contact angles, and the total depth of the concavity is quantified. In section 7, we consider the comparison of theory and experiment; a relatively simple procedure for data processing is developed. It is based on the use of tabulated theoretical dependencies, which are given in the Supporting Information for this article.

## 2. Experiment

The experiments were analogous to those described in ref 37. The water phase was pure deionized water or an aqueous solution of NaCl. The oil phase was tetradecane, with density $\rho_n = 0.763$ g/cm$^3$, dielectric constant $\epsilon_n = 2.04$, and interfacial tension against water $\gamma = 52.2$ mN/m. The experiments were carried out at 23 °C. As solid particles, we used silanized glass spheres of density $\rho_p = 2.62$ g/cm$^3$ and dielectric constant $\epsilon_p = 3.97$. The procedure of the silanization of the particles is described in ref 37.

The experimental cell is a rectangular glass box of sides from optical plane−parallel plates. The height of the cell is 55 mm. The horizontal cross section of the cell has dimensions of 80 mm × 25 mm, with both of them being markedly greater than the characteristic capillary length, $q^{-1} = (\Delta\rho g/\gamma)^{-1/2}$; the latter is 4.7 mm for the tetradecane/water interface. The inner walls of the cell are moderately hydrophobized (contact angle ≈ 80° across water). Thus, a slightly concave tetradecane/water or air/water meniscus is formed, which decays exponentially, at a relatively short distance from the walls. Thus, the meniscus around the central part of the cell is horizontal.

The observations were carried out by means of a horizontal microscope equipped with a long-focus objective and connected to a monitor and video-recording system. In the absence of the particle, a horizontal interface was seen. After inserting the particle, we observed deformations of the interface (deviations from planarity), as in the photograph in Figure 2.

We digitized the $(x, z)$ coordinates of a series of points located on the left- and right-hand-side meniscus profiles of a given video frame (Figure 2). To remove the undesired influence of an occasional

(38) Oettel, M.; Domínguez, A.; Dietrich, S. Private communication.
(39) Oettel, M.; Domínguez, A.; Dietrich, S. *Phys. Rev. E* **2005**, *71*, 051401.
(40) Nayfeh, A. H. *Perturbation Methods*; Wiley: New York, 1973.
(41) Foret, L.; Würger, A. *Phys. Rev. Lett.* **2004**, *92*, 058302.
(42) Würger, A.; Foret, L. *J. Phys. Chem. B* **2005**, *109*, 16435−16438.

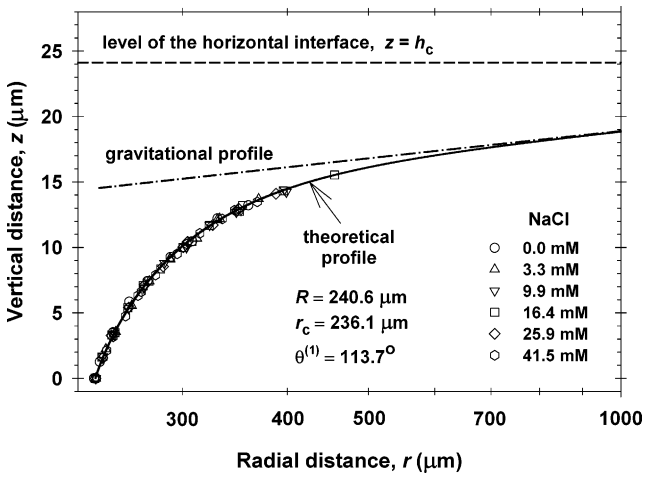


**Figure 3.** Meniscus shape, $z(r)$, around a silanized glass particle at the water−tetradecane interface. $R$ and $r_c$ are the particle and contact-line radii; $\theta^{(1)}$ is the goniometrically measured contact angle. The symbols are digitized points on the meniscus profile taken from photographs of the same particle at various NaCl concentrations. The solid line is the theoretical profile (section 3). The dashed−dotted line is the gravitational profile, calculated from eqs 2.1 and 5.3, which shows the hypothetic shape of the meniscus if electrostatic effects are missing. The dashed line is the level of the horizontal nondisturbed oil−water interface far from the particle. The difference between the theoretical and gravitational profiles represents the electric deformation of the fluid interface, $\zeta^{(el)}(r)$.

small tilt of the $x$ axis on the photograph with respect to the actual horizontal direction, we slightly rotated the axes of the $(x, z)$ coordinate system until achieving the best agreement of the left- and right-hand-side profiles for the same photograph. In most of our previous experiments,[37] only the angle $\psi_c$ was measured from the video frames. For the needs of the present article, we also digitized the meniscus profiles in these video frames. For all digitized profiles $z$ versus $r$ (see, for example, Figure 3), we applied the procedure described in section 7 to obtain $\sigma_{pn}$ and $\theta$.

As in ref 37, we did not observe any effect of the NaCl concentration in water. The latter was varied by injecting known portions of concentrated NaCl solution into the aqueous phase. An example is shown in Figure 3, where the symbols denote digitized points from the left and right profiles of six photographs of the same particle at six different NaCl concentrations denoted in the Figure. The dashed−dotted line in Figure 3 represents the gravitational meniscus profile (i.e., the hypothetical meniscus profile if electric effects were absent). The latter profile was computed with the help of eq 1.4:

$$\zeta^{(g)}(r) = -\frac{F^{(g)}K_0(qr)}{2\pi\gamma qr_c K_1(qr_c)} \approx -\frac{F^{(g)}}{2\pi\gamma}K_0(qr) \qquad (2.1)$$

In Figure 3, the curve $\zeta^{(g)}(r)$ is shifted along the vertical axis such as to coincide with the horizontal interface far from the particle for $r \to \infty$. The difference between the gravitational profile and the experimental points demonstrates the effect of the electric field on the meniscus shape. Because the variation of the NaCl concentration produces no effect, we can conclude that the electric charges are located at the particle−tetradecane boundary and that the electrostatic interaction between the particle and the oil−water interface occurs across the oily phase. From the best fit of the experimental data by the exact numerical solution for the meniscus profile (see the continuous curve in Figure 3 and section 7), we determined the surface charge density at the particle−oil interface, $\sigma_{pn} = 67.9\ \mu C/m^2$.

The data processing procedure and additional experimental data are given in section 7. The theoretical description of the meniscus profile and a more detailed discussion of Figure 3 can be found in section 3.

## 3. Theoretical Calculation of the Meniscus Profile

One can calculate the meniscus profile, $\zeta(r)$, by using three different approaches. (i) One could solve the partial differential equations of the electrostatic problem *numerically*, as in ref 37. (ii) One could solve the electrostatic boundary problem *analytically*, with the help of the Mehler−Fock integral transformation, as described in ref 43. (iii) One could describe the meniscus profile with simple *interpolation formula*, whose parameters are tabulated; see eq 3.8 and Tables A−D in the Supporting Information for this article. In subsections 3.1, 3.2, and 3.3, we consider these three different approaches separately.

**3.1. Numerical Solution of the Electrostatic Boundary Problem.** This approach is described in section 5 of ref 37. Initially, we used a second-order difference scheme with a grid of 101 × 101 subdomains. The numerical results are coincident (but the computations are longer) if a grid with 201 × 201 subdomains is used. Furthermore, we solved the same problem by means of the alternating direction implicit (ADI) method[44] using the general three-level scheme with 2001 × 2001 subdomains. The latter numerical method is different from that used in ref 37, but the results for $p_{el}(r)$ obtained by the two procedures coincide, as should be expected. The numerical procedures yield the electric field, and the electric pressure, $p_{el}$, exerted at the oil−water interface

$$p_{el}(x_1) \equiv -\frac{\epsilon_n}{8\pi}E_z^2|_{z=0} = -\frac{2\pi\sigma_{pn}^2}{\epsilon_n}G(x_1, \theta, \epsilon_{pn}) \qquad (3.1)$$

where

$$x_1 = \frac{r_c}{r} \text{ and } \epsilon_{pn} = \frac{\epsilon_p}{\epsilon_n} \qquad (3.2)$$

As usual, $\theta$ is the contact angle (Figure 1); $E_z$ is the $z$ component of the electric-field intensity; and the dimensionless function $G(x_1, \theta, \epsilon_{pn})$ is determined by numerical solution of the electrostatic boundary problem. Note that $G$ is independent of $r_c$ and $\sigma_{pn}$. From the values of $G$, we can calculate $p_{el}(r)$ with the help of eqs 3.1 and 3.2 for each set of specific values of $r_c$, $\sigma_{pn}$, $\theta$, $\epsilon_p$, and $\epsilon_n$. Finally, having determined $p_{el}$, we compute the meniscus profile, $\zeta(r)$, either by numerical solution of eq 1.6 or by means of eq 5.21 below.

The advantage of this method is that it is based on a relatively simple mathematical apparatus at the cost of application of complex numerical methods, which need longer computational time, or the use of a fast computer.

**3.2. Use of the Mehler−Fock Integral Transform.** As demonstrated in ref 43, the application of the Mehler−Fock integral transform reduces the partial differential equations of the electrostatic boundary problem to ordinary differential equations, which can be easily solved. The execution of the inverse integral transform leads to a Fredholm integral equation of the second kind. The mathematical analysis in ref 43 yields the following expression for $p_{el}$

$$p_{el}(x_1) = -\frac{2\pi\sigma_{pn}^2}{\epsilon_n}\frac{x_1^6}{(1-x_1)^{2-2\nu}}[J(x_1, \theta, \epsilon_{pn})]^2 \qquad (3.3)$$

where $J$ is a dimensionless function and $\nu$ is the smallest positive root of the equation[43]

$$\sin[(2\pi - \theta)\nu] = \beta \sin(\theta\nu) \qquad (3.4)$$

where $\beta = (\epsilon_{pn} - 1)/(\epsilon_{pn} + 1)$. Note that the smallest positive

root of eq 3.4 is always between 0.5 and 1.0. For this reason, $p_{el}$ has an integrable divergence at the contact line ($x_1 = 1$). At long distances from the particle ($x_1 \to 0$), the electric pressure vanishes, $p_{el} \propto x_1^6$. $J(x_1, \theta, \epsilon_{pn})$ is a function of bounded variation, which can be calculated from the expression[43]

$$J(x_1, \theta, \epsilon_{pn}) = \frac{2^{3/2}}{(1+x_1)^{3/2}(1-x_1)^{1/2+\nu}} \int_0^\infty \frac{\tau \Psi_s(\tau)}{\sinh[(\pi-\theta)\tau]} \times P_{-1/2+i\tau}(\cosh\eta)\, d\tau \quad (3.5)$$

where

$$\cosh\eta = 1 + \frac{2x_1^2}{1-x_1^2} \quad (3.6)$$

$P_{-1/2+i\tau}$ is the Legendre function of the first kind; $\tau$ is an integration variable; $i$ is the imaginary unit; and $\Psi_s(\tau)$ is the Mehler−Fock image of the dimensionless surface potential at the particle−oil interface. $\Psi_s(\tau)$ is calculated to high precision as a solution of the integral equation of Fredholm, which is solved by iterations; for details, see section 5.1 in ref 43. Having determined $p_{el}$ from eqs 3.3−3.6, we can compute the meniscus profile, $\zeta(r)$, by a numerical solution of eq 1.6. Alternatively, one could compute $\zeta(r)$ with the help of eqs 2.1, 3.7, and 5.22.

The advantage of the latter method for calculating $\zeta(r)$ is that the computations are much faster than those described in section 3.1. As demonstrated in ref 43 (Figures 5 and 12 therein), the two methods give numerically coinciding results. Most of the numerical results reported in the present article are obtained by means of the method based on eqs 3.3−3.6.

**3.3. Interpolation Formula for the Meniscus Profile.** The procedures for calculating $\zeta(r)$ described in sections 3.1 and 3.2 use complex numerical methods and mathematical apparatus. For the needs of fast estimates and experimental data processing, we obtained a simpler interpolation formula, eq 3.8. As demonstrated in sections 5.3 and 6.1, for small particles, $(qr_c)^2 \ll 1$, the meniscus profile can be expressed as a superposition of electric and gravitational profiles

$$\zeta(r) = \zeta^{(el)}(r) + \zeta^{(g)}(r) \quad (3.7)$$

where $\zeta^{(g)}$ is given by eq 2.1 and $\zeta^{(el)}$ can be calculated from the expression

$$\zeta^{(el)}(r) = \frac{2\pi\sigma_{pn}^2 r_c^2}{\epsilon_n \gamma}(\hat{Z}^{(el)}(x_1) - H_c^{(el)}) \quad (3.8a)$$

$$\hat{Z}^{(el)} \equiv \frac{H_c^{(el)}}{a + bx_1^2}[a(1-x_1^8) + bx_1^2(1-x_1^6)] - x_1^4(1-x_1^2)\frac{1+cx_1^2}{a+bx_1^2} \quad (3.8b)$$

where, as usual, $x_1 = r_c/r$; the coordinate origin is fixed such that $\zeta(r \to \infty) = 0$. Equation 3.8 represents a four-parameter interpolation formula. Coefficients $a$, $b$, $c$, and $H_c^{(el)}$ have been determined by fitting the numerical data for $\zeta^{(el)}$ obtained by means of the procedure in section 3.2. These coefficients are tabulated for various $\theta$ and $\epsilon_{pn}$ values; see Tables A−D in the Supporting Information for this article. For all $0 \le x_1 \le 1$ and $0.125 \le \epsilon_{pn} \le 8$, the relative error of this interpolation formula is smaller than 0.68% for $5° < \theta < 30°$, smaller than 0.5% for $30° < \theta < 150°$, and smaller than 1.0% for $150° < \theta < 165°$. Equation 3.8b was specially designed to provide the best accuracy close to the contact line ($r \to r_c$; $x_1 \to 1$), where the meniscus slope angle, $\psi_c$, and the contact angle, $\theta$, are defined.

Thus, for given $\theta$ and $\epsilon_{pn}$ values, one first determines coefficients $a$, $b$, $c$, and $H_c^{(el)}$ from Tables A−D (Supporting Information); the four-point interpolation formula, eq 7.16, is convenient for application. Then, for a given value of $\sigma_{pn}$ one can calculate $\zeta(r)$ with the help of eqs 3.7 and 3.8.

Alternatively, if experimental points for the meniscus profile are available, such as those in Figure 3, then one can fit the data with the help of eq 3.8, as explained in section 7.2.

At the contact line, $x_1 = 1$, we have $\hat{Z}^{(el)} = 0$, and eq 3.8a indicates that $H_c^{(el)}$ is the dimensionless electrostatic contribution to the depth of the concavity formed by the particle; see also eq 6.3. In the other limit, $x_1 \to 0$, eq 3.8 gives $\zeta^{(el)} \propto -x_1^4/a$; see also eq 5.24.

**3.4. Discussion.** The continuous line in Figure 3 represents the theoretical meniscus profile, which could be drawn by either of the procedures described in section 3.1, 3.2, or 3.3. The three different procedures give practically coinciding results. The depth of the concavity created by the particle is

$$h_c \equiv -\zeta(r_c) \quad (3.9)$$

$h_c$ is the distance between the planes of the contact line and the horizontal fluid interface far from the particle (Figure 3). The most important conclusions from Figure 3 are (i) that the electric forces create a concavity (dimple) of significant depth in the fluid interface around the particle and (ii) that the effect of the electric forces on $\zeta(r)$ disappears for $r > 3r_c$. At greater distances ($r > 3r_c$), the meniscus shape is governed by the gravitational deformation, $\zeta^{(g)}$, alone. In other words, the electric field produces a deformation of medium range: it is neither long-ranged (significant for $r \gg r_c$, as the gravity-induced capillary force) nor short-ranged (significant only for $r - r_c \ll r_c$, as the van der Waals attraction). (Note that the range of the electric-field-induced deformation depends on the contact angle; the range is longer for greater contact angles; see section 6.1.)

As mentioned above, the lateral capillary force between two attached particles is due to the overlap of the dimples formed around them.[29−32] Correspondingly, the range of this capillary force is determined by the range of the interfacial deformations. Thus, we could expect that the capillary interaction engendered by the electrodipping force, $F^{(el)}$, is of medium range. The profile in Figure 3 indicates that the capillary interaction between two floating particles (the electric-field-induced capillary attraction[20]) could be very strong for $r < 3r_c$. (For contact angle ~150°, the respective range is $r < 5r_c$; see section 6.1.)

Indications of the action of an attractive force of (at least) medium range were recently observed by Horozov et al. for silica particles at oil−water[23,27] and air−water[28] interfaces. The charged particles aggregate despite the presence of a strong electrostatic (Coulombic and dipolar) repulsion between them. This shows the presence of an attractive force, which is able to overcome the electrostatic repulsion and to produce particle aggregation. It is important to note that the aggregated particles are not in close contact but stay well separated at equilibrium distances beyond the range of the van der Waals attraction.[27] As suggested by Horozov et al.,[27,28] a possible origin of the observed attraction can be the capillary force due to the undulated contact

(43) Danov, K. D.; Kralchevsky, P. A. *J. Colloid Interface Sci.*, in press, 2006.
(44) Fletcher C. A. J. *Computational Techniques for Fluid Dynamics 1. Fundamental and General Techniques*, 2nd ed.; Springer-Verlag: Berlin, 1991; pp 251−271.

line.[18,45−47] In refs 27 and 28, the particle−oil (air) interface has been electrically charged; therefore, another possible explanation of the observed aggregation could be the action of electric-field-induced capillary attraction related to electric deformations of the fluid interface (e.g., Figure 3).

In Figure 3, the gravitational deformation, $\zeta^{(g)}$, described by eq 2.1 dominates the meniscus profile for $r > 3r_c$. For $r_c = 200-300$ $\mu$m, as in our present experiments, $\zeta^{(g)}$ gives rise to a long-range gravity-induced capillary attraction between two floating particles. In contrast, for smaller particles, $r_c < 5-10$ $\mu$m, the effect of $\zeta^{(g)}$ becomes negligible.[32]

A second point that should be discussed is the expression for $p_{el}(r)$. In our previous article,[37] the numerical data for $p_{el}(r)$ have been fitted by means of a semiempirical formula, eq 3.7, therein, which could be obtained from eq 3.3 if we formally substitute

$$J^2 \approx \frac{\lambda F^{(el)} \epsilon_n}{\pi^2 r_c^{\,2} \sigma_{pn}^{\,2}} = \text{const} \qquad (3.10)$$

where $\lambda = (3+\mu)(2+\mu)(1+\mu)\mu/24$ and $\mu = 2\nu - 1$. However, the general theory in ref 43 shows that $J$ depends on $x_1$. Despite the fact that the latter dependence is not strong, it should be taken into account when calculating the meniscus profile $\zeta(r)$ by integrating eq 1.6. For this reason, it is not recommended to use the semiempirical formula, eq 3.7 in ref 37, for the computation of $\zeta(r)$.

Another point that deserves discussion and is related to the comparison of theory and experiment is the following. When calculating the electrostatic field in refs 37 and 43, as a zeroth-order approximation it is assumed that the water−nonpolar fluid boundary is planar. Then, the electric-field intensity and $p_{el}$ are calculated. Finally, the calculated $p_{el}$ is substituted into the Laplace equation, eq 1.6, and the interfacial deformation (deviation from planarity), $\zeta(r)$, is determined (e.g., ref 37). In other words, when solving the electrostatic boundary problem, it was assumed (in the zeroth-order approximation) that $\theta = \alpha$ (Figure 1) and then $\zeta(r)$ was determined as a first-order correction for the same $r_c$. For a deformed interface, we have $\theta = \alpha + \psi_c$, and we can determine each of the latter three angles from photographs (such as Figure 2) by goniometric measurements. When comparing the experimental meniscus profile, $\zeta(r)$, with theory and determining the angle as an adjustable parameter (section 7), one obtains a value that is very close to the experimental angle $\theta$ rather than to $\alpha$; compare angles $\theta^{(1)}$ and $\theta^{(e)}$ in section 7. This result is related to the fact that the meniscus deformation is very sensitive to the angle of the wedge-shaped domain near the contact line, which is filled with the nonpolar fluid (Figure 1). The main electric interaction between the particle and the oil−water interface occurs across this wedge-shaped domain. The angle of the wedge ($\pi - \theta$, Figure 1) is determined by $\theta$, and because of that, the comparison of theory and experiment gives $\theta$ (rather than $\alpha$) when the angle is obtained as an adjustable parameter. For this reason, in eqs 3.1 and 3.3−3.5 the angle is denoted $\theta$ instead of $\alpha$ despite the fact that the underlying electrostatic theory assumes (as an approximation) that $\theta = \alpha$. In fact, the contact angle $\theta$ can be determined in three different ways: (i) goniometrically, from a photograph such as that in Figure 2 (section 7.1); (ii) as an adjustable parameter from fits of data for the meniscus profile (section 7.2); and (iii) from the slope of the theoretical curve (representing the best fit), $(d\zeta/dr)_{r=r_c}$ (section 7.3). The respective three values of the contact angle are denoted $\theta^{(1)}$, $\theta^{(e)}$, and $\theta^{(2)}$, the latter being the most reliable; see section 7.

## 4. Range of the Meniscus Electric Deformation

**4.1. Estimate of the Range of $p_{el}$.** According to eq 6.6 in ref 37, the electric force exerted on the particle, $F^{(el)}$, must be equal to the integral of $p_{el}$ over the oil−water (air−water) interface:

$$F^{(el)} = -2\pi \int_{r_c}^{\infty} dr\, r\, p_{el}(r) \qquad (4.1)$$

Let us check how far from the particle we have to integrate in order to satisfy eq 4.1 with a sufficiently small error, equal to $\epsilon$:

$$\frac{-2\pi \int_{r}^{\infty} dr\, r\, p_{el}(r)}{F^{(el)}} = \epsilon \qquad (\epsilon \ll 1) \qquad (4.2)$$

To estimate the integral in eq 4.2, we substitute the asymptotic expression for $p_{el}$, eq 3.9 in ref 3.7:

$$p_{el}(r) \approx -\frac{2\lambda r_c^{\,4} F^{(el)}}{\pi r^6} \qquad \left(\frac{r}{r_c} \gg 1\right) \qquad (4.3)$$

From eqs 4.2 and 4.3, we get

$$\frac{r}{r_c} = \left(\frac{\lambda}{\epsilon}\right)^{1/4} \qquad (4.4)$$

With $\lambda = 0.482$ (see ref 37), eq 4.4 yields

$$\epsilon = 0.01 \text{ for } \frac{r}{r_c} = 2.6 \qquad (4.5)$$

$$\epsilon = 0.001 \text{ for } \frac{r}{r_c} = 4.7 \qquad (4.6)$$

If eq 4.2 is used as a measure of the range of the electric force, then eqs 4.5 and 4.6 indicate that the effect of the electric field on $\zeta(r)$ practically disappears at $r/r_c > 4$. This conclusion is in agreement with the results shown in Figure 3.

**4.2. Long-Range Asymptotics of the Meniscus Profile.** Let us encircle the floating particle with an imaginary cylinder (Figure 4), which has a sufficiently large diameter, $r_1$, so that the relation

$$-2\pi \int_{r_c}^{r_1} dr\, r\, p_{el}(r) \approx F^{(el)} \qquad (4.7)$$

is fulfilled with good accuracy; see eqs 4.5 and 4.6. Because the effect of $p_{el}$ is negligible for $r > r_1$, eq 1.6 reduces to eq 1.1, which has the following solution:

$$\zeta(r) = \frac{-F_1}{2\pi\gamma q r_1 K_1(qr_1)} K_0(qr) \approx \frac{F_1}{2\pi\gamma} \ln\left(\frac{\gamma_e q r}{2}\right) \qquad (r \geq r_1) \quad (4.8)$$

Here, for $(qr)^2 \ll 1$, we have used the asymptotics given by eq 1.5 and the boundary condition at the cylinder surface (Figure 4):

$$\frac{d\zeta}{dr}\Big|_{r=r_1} = \frac{F_1}{2\pi\gamma r_1} \qquad (4.9)$$

$F_1$ is the force acting on the selected cylinder of radius $r_1$. In view of eq 4.7, the electric field is "closed" inside this cylinder (i.e., its flux across the cylinder's walls is (approximately) equal to

(45) Kralchevsky, P. A.; Denkov, N. D.; Danov, K. D. *Langmuir* **2001**, *17*, 7694−7705.
(46) Danov, K. D.; Kralchevsky, P. A.; Naydenov, B. N.; Brenn, G. *J. Colloid Interface Sci.* **2005**, *287*, 121−134.
(47) Loudet, J. C.; Alsayed, A. M.; Zhang, J.; Yodh, A. G. *Phys. Rev. Lett.* **2005**, *94*, 018301.

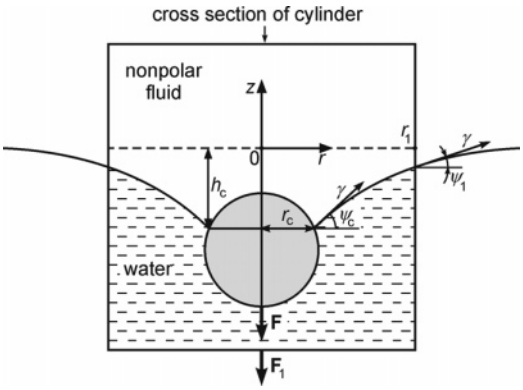


**Figure 4.** Sketch of a particle at the water−nonpolar fluid boundary. Because of force $F = F^{(g)} + F^{(el)}$ acting on the particle, the fluid interface is deformed. The particle is encircled by an imaginary vertical cylinder of radius $r_1$. The total force acting on this cylinder is denoted by $F_1$; $\gamma$ is interfacial tension; $\psi_c$ and $\psi_1$ are, respectively, the meniscus slope angles at the contact line and at the cylinder wall; $h_c$ characterizes the depth of the concavity (dimple). The magnitude of the meniscus deformation is exaggerated.

zero). Then, the magnitude of $F_1$ will be determined by the gravitational force acting on this cylinder. In such a case, an expression for $F_1$ can be deduced by buoyancy-force considerations. The same result can be obtained more easily from the Laplace equation of capillarity[48]

$$\frac{\gamma}{r}\frac{\mathrm{d}}{\mathrm{d}r}(r \sin \psi) = (\rho_w - \rho_n)g\zeta + p_{el}(r) \qquad (4.10)$$

where $\rho_w$ and $\rho_n$ are the mass densities of the water and nonpolar fluid and $\psi$ is the slope angle of the meniscus profile ($\tan \psi = {}^{\mathrm{d}\zeta}/_{\mathrm{d}r}$). Equation 1.6 is a special case (linearized form) of eq 4.10 for small meniscus slope (i.e., for $\tan^2 \psi \ll 1$). The force balances at the particle and at the cylinder (Figure 4) yield

$$2\pi\gamma r_c \sin \psi_c = F^{(g)} + F^{(el)} \qquad 2\pi\gamma r_1 \sin \psi_1 = F_1 \quad (4.11)$$

where $\psi_1 = \psi(r_1)$ and $\psi_c = \psi(r_c)$. (The same follows from boundary conditions given by eqs 1.3 and 4.9 for $\sin \psi \approx \tan \psi = {}^{\mathrm{d}\zeta}/_{\mathrm{d}r}$). By integrating eq 4.10, we obtain

$$2\pi\gamma(r_1 \sin \psi_1 - r_c \sin \psi_c) = 2\pi(\rho_w - \rho_n)g\int_{r_c}^{r_1} \mathrm{d}r\, r\, \zeta(r) + 2\pi\int_{r_c}^{r_1} \mathrm{d}r\, r\, p_{el}(r) \quad (4.12)$$

Next, we substitute eqs 4.7 and 4.11 into eq 4.12; the result reads

$$F_1 = F^{(g)} - (\rho_w - \rho_n)gV_m \qquad (4.13)$$

where $V_m$ denotes the volume confined between the meniscus and the horizontal plane $z = 0$ (Figure 4):

$$V_m = -2\pi\int_{r_c}^{r_1} \mathrm{d}r\, r\, \zeta(r) \qquad (4.14)$$

Note that $V_m > 0$ because for the present choice of the coordinate system we have $\zeta \le 0$. In view of eq 4.13, we have

$$F_1 < F^{(g)} \text{ but } F_1 \approx F^{(g)} \text{ because } V_m \ll V_p \qquad (4.15)$$

where $V_p$ is the particle volume and $F^{(g)} \propto V_p$ (see below). Equations 4.13 and 4.15 show that the logarithmic prefactor in eq 4.8 (describing the meniscus shape in the "outer region", $r > r_1$) cannot be greater than $F^{(g)}$, and it certainly does not contain a contribution from $F^{(el)}$. In fact, the prefactor is very close to $F^{(g)}$ because the term with $V_m$ in eq 4.13 is comparatively small. Thus, setting $F_1 \approx F^{(g)}$ into eq 4.8, we obtain

$$\zeta(r) \approx \frac{F^{(g)}}{2\pi\gamma}\ln\left(\frac{\gamma_e q r}{2}\right) \qquad (r \ge r_1) \qquad (4.16)$$

In other words, for $r \ge r_1$ the logarithmic prefactor is determined solely by $F^{(g)}$, in agreement with our results in Figure 3. Note that the linear portion on the right-hand side of the plot in Figure 3, where the solid and dashed−dotted curves coincide, corresponds to the logarithmic dependence in eq 4.16. The coincidence of the latter two curves is also indirect proof that in the considered case $V_m \ll V_p$ and that the difference between $F_1$ and $F^{(g)}$ is small (eq 4.15).

The fact that the long-range asymptotics of $\zeta(r)$ is dominated by $F^{(g)}$ (eq 4.16) is in agreement with the conclusion of Oettel et al.[39] and with part of the conclusions of Megens and Aizenberg.[36] The latter authors wrote that if there is any effect it is too short-ranged "so overall, there is no attraction at all."[36] In fact, this could happen if surface charges are present only at the particle−water boundary and if the concentration of electrolyte in the aqueous phase is sufficiently high. However, this is certainly not the case when surface charges of sufficiently high density, $\sigma_{pn}$, are present at the particle−nonpolar fluid boundary. In the latter case, the interfacial deformation is of medium range (Figure 3 and section 7.4).

## 5. Superposition of the Electric and Gravitational Deformations

Here, our aim is to prove that for small particles ($(qR)^2 \ll 1$) for which the meniscus slope is small and the Laplace equation of capillarity can be linearized the meniscus profile can be presented as a superposition of the electric and gravitational deformations, $\zeta(r) = \zeta^{(el)}(r) + \zeta^{(g)}(r)$; see eq 3.7. First, we will consider the expressions for $\zeta^{(g)}(r)$ and $\zeta^{(el)}(r)$ separately.

**5.1. Gravitational Deformation.** In the considered case of small meniscus slope, the gravitational deformation caused by a floating particle (Figure 1) is described by eq 2.1. Close to the contact line, where $(qr)^2 \ll 1$, the asymptotic expression for $K_0$, eq 1.5, can be used, and eq 2.1 acquires a simpler form:

$$\zeta^{(g)}(r) \approx \frac{F^{(g)}}{2\pi\gamma}\ln\left(\frac{qr\gamma_e}{2}\right) \text{ at } (qr)^2 \ll 1 \qquad (5.1)$$

Because of the logarithmic dependence in eq 5.1, $\zeta^{(g)}(r)$ looks like a straight line when $r$ is plotted on a log scale; see Figure 3. The gravitational force, $F^{(g)}$, acting on the particle, is equal to the particle weight minus the buoyancy force due to the fluid displaced by the particle and the encircling meniscus:[49,50]

$$F^{(g)} = g[(\rho_p - \rho_w)V_w + (\rho_p - \rho_n)V_n - (\rho_w - \rho_n)\pi r_c^2 h_c] \qquad (5.2)$$

Here, $V_w$ and $V_n$ are the portions of the particle volume, which are immersed, respectively, in the water and in the nonpolar fluid. For the considered small particles, the term with $h_c$ is much smaller than the other two terms on the right-hand side of eq 5.2, and it can be neglected:

(48) Princen, H. M. The Equilibrium Shape of Interfaces, Drops, and Bubbles. In *Surface and Colloid Science*; Matijevič, E., Ed.; Wiley: New York, 1969; Vol. 2, p 1.

(49) Nutt, C. W. *Chem. Eng. Sci*. **1960**, *12*, 133−141.

(50) Ivanov, I. B.; Kralchevsky, P. A.; Nikolov, A. D. *J. Colloid Interface Sci.* **1986**, *112*, 97−107.

$$F^{(g)} \approx g[(\rho_p - \rho_w)V_w + (\rho_p - \rho_n)V_n] \quad (5.3)$$

Furthermore, expressing $V_w$ and $V_n$ in terms of $R$ and cos α (Figure 1) and using the relationship $F^{(g)} = 2\pi r_c \gamma \sin \psi_c^{(g)}$ we obtain from eq 5.3[45]

$$\sin \psi_c^{(g)} \approx \frac{(qR)^2}{6 \sin \alpha}(4D_\rho - 2 - 3\cos \alpha + \cos^3 \alpha) \quad (5.4)$$

Here, $D_\rho = (\rho_p - \rho_n)/(\rho_w - \rho_n)$, and $\psi_c^{(g)}$ is the gravitational meniscus slope angle at the contact line. Equation 5.4 enables one to estimate whether the condition for a small meniscus slope, $(\sin \psi_c^{(g)})^2 \ll 1$, is satisfied for given $R$, α, and mass densities $\rho_p$, $\rho_w$, and $\rho_n$.

**5.2. Electric Deformation.** For small spherical particles ($R \leq 5\,\mu$m), such as those used in many experiments, the gravitational force, $F^{(g)}$, and the gravitational deformation of the meniscus, $\zeta^{(g)}$, are negligible.[32] In other words, if there were no electric effects, then the meniscus around the floating sphere would be planar, $\zeta \approx 0$. (Here, we assume that undulations of the contact line due to surface roughness or inhomogeneity are missing.) Then, the deformation of the water−nonpolar fluid interface, $\zeta^{(el)}(r)$, is due only to the electric forces. The latter deformation is described by eq 1.6 with a neglected gravitational term, $q^2\zeta$:

$$\frac{1}{r}\frac{d}{dr}\left(r\frac{d\zeta^{(el)}}{dr}\right) = \frac{1}{\gamma}p_{el}(r) \quad (5.5)$$

As demonstrated below, eq 5.5 and its solution, eq 5.9, also describe the electric interfacial deformation for larger particles, for which $\zeta^{(g)}$ is not zero. We seek a solution of eq 5.5, which satisfies the boundary conditions

$$\lim_{r\to\infty}\left(r\frac{d\zeta^{(el)}}{dr}\right) = 0 \quad (5.6)$$

$$\left(\frac{d\zeta^{(el)}}{dr}\right)_{r=r_c} = \frac{F^{(el)}}{2\pi\gamma r_c} \quad (5.7)$$

Integrating eq 5.5, along with eq 5.6, we obtain

$$-r\frac{d\zeta^{(el)}}{dr} = \frac{1}{\gamma}\int_r^\infty d\hat{r}\, \hat{r}\, p_{el}(\hat{r}) \quad (5.8)$$

One can check that if we set $r = r_c$ in eq 5.8 and substitute the integral from eq 4.1 we get exactly the boundary condition, eq 5.7. In other words, the boundary condition, eq 5.7, is automatically satisfied by the first integral, eq 5.8. A subsequent integration of eq 5.8 yields the meniscus profile:

$$\zeta^{(el)}(r) = \frac{1}{\gamma}\int_r^\infty \frac{d\tilde{r}}{\tilde{r}}\int_{\tilde{r}}^\infty d\hat{r}\, \hat{r}\, p_{el}(\hat{r}) = \frac{1}{\gamma}\int_r^\infty d\hat{r}\, \hat{r}\, p_{el}(\hat{r}) \ln\left(\frac{\hat{r}}{r}\right) \quad (5.9)$$

Here, in the last step we have applied integration by parts and have used the boundary condition $\zeta^{(el)}(\infty) = 0$. Because $p_{el}(r) \propto 1/r^6$ for $r \to \infty$, the integrals in eq 5.9 are convergent, and $\zeta$ tends to zero at $r \to \infty$; see eq 5.24. Keeping in mind that $p_{el} < 0$, eq 5.9 implies that $\zeta^{(el)}$ is negative.

In summary, eq 5.9 is the physical solution of eq 5.5, which tends toward a planar interface at long distances (no electric deformation) and satisfies the force balance at the contact line, eq 5.7.

**5.3. Combined Gravitational and Electric Deformation.** This case corresponds to our experimental situation; see, for example, Figure 3. The equation for the meniscus profile, eq 1.6, is an inhomogeneous modified Bessel equation that has a standard solution:[51]

$$-\zeta(r) = \frac{1}{\gamma}I_0(qr)\int_r^\infty d\hat{r}\, \hat{r}\, p_{el}(\hat{r})\, K_0(q\hat{r}) + \frac{1}{\gamma}K_0(qr)\left[A + \int_{r_c}^r d\hat{r}\, \hat{r}\, p_{el}(\hat{r})\, I_0(q\hat{r})\right] \quad (5.10)$$

See also ref 39. Here, $\hat{r}$ is integration variable; $A$ is an integration constant, and $I_0$ and $K_0$ are the modified Bessel functions of zeroth order.[33−35] Equation 5.10 satisfies the boundary condition $\zeta \to 0$ for $r \to \infty$. From the second boundary condition, eq 1.3, we determine $A$ in eq 5.10

$$A = \frac{\dfrac{F}{2\pi r_c} + qI_1(qr_c)\displaystyle\int_{r_c}^\infty dr\, r\, p_{el}(r)\, K_0(qr)}{qK_1(qr_c)} \quad (5.11)$$

where $I_1$ and $K_1$ are modified Bessel functions of first order and $F = F^{(g)} + F^{(el)}$. For submillimeter particles, we have $(qr_c)^2 \ll 1$; consequently, $I_1(qr_c) \approx qr_c/2$ and $K_1(qr_c) \approx 1/(qr_c)$. Then, eq 5.11 simplifies to

$$A \approx \frac{F}{2\pi} + \frac{1}{2}(qr_c)^2\int_{r_c}^\infty dr\, r\, p_{el}(r)\, K_0(qr) \quad (5.12)$$

For $(qr_c)^2 \ll 1$, the integral term in eq 5.12 is negligible, and eq 5.10 acquires the form

$$\zeta(r) = -\frac{1}{\gamma}I_0(qr)\int_r^\infty d\hat{r}\, \hat{r}\, p_{el}(\hat{r})\, K_0(q\hat{r}) - K_0(qr)\left[\frac{F}{2\pi\gamma} + \frac{1}{\gamma}\int_{r_c}^r d\hat{r}\, \hat{r}\, p_{el}(\hat{r})\, I_0(q\hat{r})\right] \quad (5.13)$$

In principle, eq 5.13 solves the problem. Its application to the calculation of the meniscus profile is described in section 5.4.

For the small particles considered in the present study, eq 5.13 could be further simplified. To describe the meniscus shape near the contact line, $(qr)^2 \ll 1$, we can set $I_0(qr) \approx 1$. Then eq 5.13 reduces to

$$\zeta(r) \approx -\frac{1}{\gamma}\int_r^\infty d\hat{r}\, \hat{r}\, p_{el}(\hat{r})\, K_0(q\hat{r}) - K_0(qr)\left[\frac{F}{2\pi\gamma} + \frac{1}{\gamma}\int_{r_c}^r d\hat{r}\, \hat{r}\, p_{el}(\hat{r})\right] \quad (5.14)$$

In view of eq 4.1, we have

$$\int_{r_c}^r d\hat{r}\, \hat{r}\, p_{el}(\hat{r}) = -\frac{F^{(el)}}{2\pi} - \int_r^\infty d\hat{r}\, \hat{r}\, p_{el}(\hat{r}) \quad (5.15)$$

Because $F - F^{(el)} = F^{(g)}$, from eqs 5.14 and 5.15 we obtain

$$\zeta(r) \approx -\frac{1}{\gamma}\int_r^\infty d\hat{r}\, \hat{r}\, p_{el}(\hat{r})[K_0(q\hat{r}) - K_0(qr)] - \frac{F^{(g)}}{2\pi\gamma}K_0(qr) \quad (5.16)$$

Because $p_{el}(r) \propto 1/r^6$ for $r \to \infty$, only the behavior of $K_0$ at short distances gives an essential contribution to the integral in eq 5.16. Thus, by substituting $K_0(qr) \approx -\ln(\gamma_e qr/2)$ into eq 5.16 one obtains

(51) Kamke, E. *Differential Equations. Solution Methods and Solutions*; Teubner: Stuttgart, Germany, 1983.

$$\zeta(r) \approx \frac{1}{\gamma}\int_r^\infty \mathrm{d}\hat{r}\, \hat{r}\, p_{\mathrm{el}}(\hat{r}) \ln\left(\frac{\hat{r}}{r}\right) - \frac{F^{(\mathrm{g})}}{2\pi\gamma}K_0(qr) = \zeta^{(\mathrm{el})} + \zeta^{(\mathrm{g})} \tag{5.17}$$

where in the last step we used eqs 2.1 and 5.9. In section 5.4, we demonstrate that for the considered small particles, $(qr_c)^2 \ll 1$, the $\zeta(r)$ dependence calculated from the approximated eq 5.17 agrees excellently with $\zeta(r)$ calculated from the exact eq 5.13. In other words, for small particles, the meniscus shape can be expressed as a sum of pure electric and gravitational deformations, $\zeta = \zeta^{(\mathrm{el})} + \zeta^{(\mathrm{g})}$, as predicted by eq 5.17. The same is true for the depth of the concavity formed by the particle:

$$h_c \approx h_c^{(\mathrm{el})} + h_c^{(\mathrm{g})} \tag{5.18}$$

$$h_c^{(\mathrm{el})} = -\zeta^{(\mathrm{el})}(r_c) = -\frac{1}{\gamma}\int_{r_c}^\infty \mathrm{d}\hat{r}\, \hat{r}\, p_{\mathrm{el}}(\hat{r}) \ln\left(\frac{\hat{r}}{r}\right) \tag{5.19}$$

$$h_c^{(\mathrm{g})} = -\zeta^{(\mathrm{g})}(r_c) = \frac{F^{(\mathrm{g})}}{2\pi\gamma}K_0(qr_c) \tag{5.20}$$

See also eqs 3.9 and 5.17.

**5.4. Comparison of the Exact and Approximated Equations for $\zeta^{(\mathrm{el})}$.** Equation 5.13 can be also presented in the form $\zeta = \zeta^{(\mathrm{el})} + \zeta^{(\mathrm{g})}$, where $\zeta^{(\mathrm{g})}$ is defined by eq 2.1, and

$$-\zeta^{(\mathrm{el})}(r) = \frac{1}{\gamma}I_0(qr)\, K_0(qr) \times \left[\int_r^\infty \hat{r}p_{\mathrm{el}}(\hat{r})\frac{K_0(q\hat{r})}{K_0(qr)}\,\mathrm{d}\hat{r} + \int_{r_c}^r \hat{r}p_{\mathrm{el}}(\hat{r})\frac{I_0(q\hat{r})}{I_0(qr)}\,\mathrm{d}\hat{r}\right] + \frac{F^{(\mathrm{el})}}{2\pi\gamma}K_0(qr) \tag{5.21}$$

Equation 5.21 expresses $\zeta^{(\mathrm{el})}$ for the combined electric and gravitational deformation, and at first glance, it is very different from eq 5.9, which expresses a pure electric deformation. Our goal here is to demonstrate that for small particles, $(qr_c)^2 \ll 1$, eqs 5.9 and 5.21 give numerically identical results.

Equation 5.21 is presented in a form convenient to numerical calculations. Indeed, the ratios $K_0(q\hat{r})/K_0(qr)$ and $I_0(q\hat{r})/I_0(qr)$ are smaller that 1. In addition, for $r \to \infty$ we have $I_0(qr)\, K_0(qr) \approx 1/(2qr) \to 0$. Hence, the divergence of $I_0(qr)$ for large $r$ does not cause computational problems when eq 5.21 is applied.

To calculate $\zeta^{(\mathrm{el})}$ from eqs 5.9 and 5.21, we substituted $p_{\mathrm{el}}(r)$ from eq 3.3 and carried out the computations with the help of eqs 3.4−3.6. In particular, the combination of eqs 3.3 and 5.9 yields

$$\zeta^{(\mathrm{el})}(r) = -\frac{2\pi\sigma_{\mathrm{pn}}{}^2 r_c{}^2}{\epsilon_n\gamma}\int_0^{x_1} \frac{\hat{x}_1{}^3}{(1-\hat{x}_1)^{2-2\nu}} \times [J(\hat{x}_1, \theta, \epsilon_{\mathrm{pn}})]^2 \ln\left(\frac{x_1}{\hat{x}_1}\right)\mathrm{d}\hat{x}_1 \tag{5.22}$$

The integral in eq 5.22 is convergent. We have $0 < 2 - 2\nu < 1$, and the singularity at $x_1 \to 1$ is integrable; see eq 3.4 for the definition of $\nu$. The situation in which eq 3.3 is substituted into eq 5.21 is analogous.

It should also be noted that the dimensionless function $J$ in eq 5.22 is finite over the whole region $0 \le x_1 \le 1$. Its limiting values

$$D(\theta, \epsilon_{\mathrm{pn}}) = \lim_{x_1\to 0} J(x_1, \theta, \epsilon_{\mathrm{pn}}) \qquad C(\theta, \epsilon_{\mathrm{pn}}) = \lim_{x_1\to 1} J(x_1, \theta, \epsilon_{\mathrm{pn}}) \tag{5.23}$$

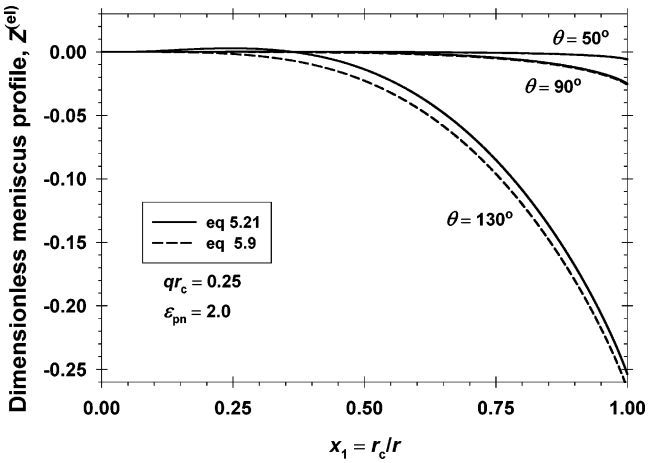


**Figure 5.** Dimensionless meniscus profile calculated from eq 5.25, in combination with eq 5.9 or 5.21, for a relatively large particle, $qr_c = 0.25$, at three values of the contact angle $\theta$. Note that eq 5.9 describes a purely electric deformation, whereas eq 5.21 accounts for the influence of gravity on the electric deformation. For $\theta = 50$ and 90°, the curves computed by means of eqs 5.9 and 5.21 practically coincide.

are calculated from the analytical solution and tabulated in ref 43, Tables 1 and 2 therein. From eqs 5.22 and 5.23, one can determine the asymptotic behavior of $\zeta(r)$ for large $r$ (small $x_1$):

$$\zeta^{(\mathrm{el})}(r) = -\frac{2\pi\sigma_{\mathrm{pn}}{}^2 r_c{}^2}{\epsilon_n\gamma}\frac{D^2}{16}x_1{}^4 \text{ for } r \gg r_c \tag{5.24}$$

Note that eq 3.8 gives an asymptotic equivalent to eq 5.24, with $D^2 = 16/a$. It is more accurate to determine $D$ from Table 1 in ref 43 than to use $a$ from Table A in the Supporting Information for this article, although the latter Table also provides a very good estimate of $D$.

In our computations, we also obtained the dimensionless meniscus profile, $Z^{(\mathrm{el})}$, which in view of eq 5.22 is defined as follows:

$$Z^{(\mathrm{el})}(x_1) \equiv \frac{\epsilon_n\gamma}{2\pi\sigma_{\mathrm{pn}}{}^2 r_c{}^2}\zeta^{(\mathrm{el})}(r) \qquad x_1 = \frac{r_c}{r} \tag{5.25}$$

We computed $Z^{(\mathrm{el})}(x_1)$ from eqs 5.9 and 5.21, where $p_{\mathrm{el}}(r)$ was substituted from eq 3.3. The numerical results for $Z^{(\mathrm{el})}(x_1)$ obtained from eqs 5.9 and 5.21 practically coincide for submillimeter particles, when $(qr_c)^2 \ll 1$. As illustrated in Figure 5, a noticeable difference between the two equations appears for relatively large particles, $qr_c = 0.25$, and for the larger contact angles, $\theta = 130°$. For the water/tetradecane interface, we have $q^{-1} = 4.7$ mm, and then $qr_c = 0.25$ corresponds to $r_c = 1.18$ mm, which is a relatively large particle. Even for such particle, eqs 5.9 and 5.21 give practically coincident profiles when $\theta = 50$ and 90° (Figure 5).

Our computations lead to the conclusion that for submillimeter particles the approximate eq 5.9 gives the same numerical results for $Z^{(\mathrm{el})}(x_1)$ as the exact eq 5.21. This result confirms that for submillimeter particles the meniscus profile can be presented as a simple superposition of the pure electric and gravitational deformations, in accordance with eq 5.17. Hereafter, all of our calculations will be based on eq 5.17.

## 6. Numerical Results and Discussion

**6.1. Comparison of the Gravitational and Electric Deformations.** To illustrate the relative effect of gravitational and electric forces on the meniscus shape, we calculated $\zeta^{(\mathrm{g})}(r)$ and

$\zeta^{(el)}(r)$ for typical parameter values corresponding to the experimental values in section 2:

$$\rho_n = 0.763\ \text{g/cm}^3 \qquad \rho_p = 2.62\ \text{g/cm}^3 \qquad \gamma = 52.2\ \text{mN/m}$$
$$\epsilon_n = 2.04 \qquad \epsilon_p = 3.97 \qquad \sigma_{pn} = 70\ \mu\text{C/m}^2 \qquad (6.1)$$

Thus, we have $\epsilon_{pn} = \epsilon_p/\epsilon_n = 1.946$. In our experiments, the greater particle radius was $R = 265\ \mu$m, which corresponds to $qR = 0.0564$ ($q^{-1} = 4.7$ mm). For such small particles, the meniscus shape can be expressed as a superposition of gravitational and electric deformation; see eq 5.17. $\zeta^{(g)}(r)$ and $\zeta^{(el)}(r)$ were calculated by means of eqs 2.1 and 5.22, respectively. To simplify the calculations, in eq 5.22 we have set $\theta = \alpha$ (Figure 1).

Figure 6 compares the calculated, purely gravitational deformation, $\zeta^{(g)}$, with the total deformation, $\zeta^{(g)} + \zeta^{(el)}$, for two angles $\alpha = 50$ and 90° and for three particle radii $R = 200$, 100, and 50 $\mu$m. The boundary condition $\zeta(\infty) = 0$ has been used. One sees that for $\alpha = 50°$ (hydrophilic particle) the electric deformation, $\zeta^{(el)}$, is relatively small, in comparison with $\zeta^{(g)}$, and is located in close proximity to the contact line. For $\alpha = 90°$, the electric deformation, $\zeta^{(el)}$, is considerable and becomes comparable to and even greater than $\zeta^{(g)}$ (Figure 6c). The magnitude of the total deformation, $\zeta^{(g)} + \zeta^{(el)}$, and the magnitude of $\zeta^{(g)}$ markedly decrease with decreasing particle radius, $R$; compare parts a−c of Figure 6.

Figure 7 compares the gravitational deformation, $\zeta^{(g)}$, with the total deformation, $\zeta^{(g)} + \zeta^{(el)}$, for hydrophobic particles at two angles $\alpha = 120$ and 150° and for three particle radii $R = 200$, 100, and 50 $\mu$m. In this case, the electric deformation, $\zeta^{(el)}$, is considerably greater than the gravitational one, $\zeta^{(g)}$. This is due to the greater total surface electric charge (greater area of the particle−oil interface) and to the specific interfacial configuration in the three-phase contact region. $\zeta^{(g)}$ is relatively small and is practically the same for $\alpha = 120$ and 150°.

It is important to note that the range of the electric interfacial deformation markedly depends on the contact angle. Thus, for $\alpha = 50$, 90, and 150°, $\zeta^{(el)}$ becomes negligible ($\zeta^{(el)}/\zeta^{(g)} \leq 2\%$ and $\zeta \approx \zeta^{(g)}$) for $r \geq 1.5r_c$, $2.5r_c$, and $5r_c$, respectively (Figures 6 and 7).

**6.2. Depth of the Concavity Produced by the Particle.** The depth of the concavity (dimple) produced by the particle, $h_c$, is a physically important parameter that is used in the procedure for determining the surface charge density, $\sigma_{pn}$, from the experimental meniscus profile $\zeta(r)$ (section 7). To calculate $h_c$, we used eqs 5.18−5.20. In particular, the substitution of eq 3.3 into eq 5.19 yields

$$h_c^{(el)} = \frac{2\pi\sigma_{pn}^2 r_c^2}{\epsilon_n \gamma}\int_0^1 \frac{x_1^3}{(1-x_1)^{2-2\nu}}[J(x_1, \theta, \epsilon_{pn})]^2 \ln\left(\frac{1}{x_1}\right) dx_1 \qquad (6.2)$$

In view of eq 5.25, the dimensionless depth of the electric-field-induced concavity is

$$H_c^{(el)}(\theta, \epsilon_{pn}) \equiv -Z^{(el)}(1) = \frac{\epsilon_n \gamma}{2\pi\sigma_{pn}^2 r_c^2} h_c^{(el)} \qquad (6.3)$$

See also eq 3.8. Figure 8 shows plots of $H_c^{(el)}$ versus $\theta$ for various values of $\epsilon_{pn}$. One sees that $H_c^{(el)}$ depends very strongly on $\theta$: it varies by 5 orders of magnitude for $5° \leq \theta \leq 175°$. However, the dependence of $H_c^{(el)}$ on $\epsilon_{pn}$ is relatively weak. Because the dependence $H_c^{(el)}(\theta, \epsilon_{pn})$ is used to determine $\sigma_{pn}$ from experimental data (section 7), it is tabulated; see Table D in the Supporting Information for this article.

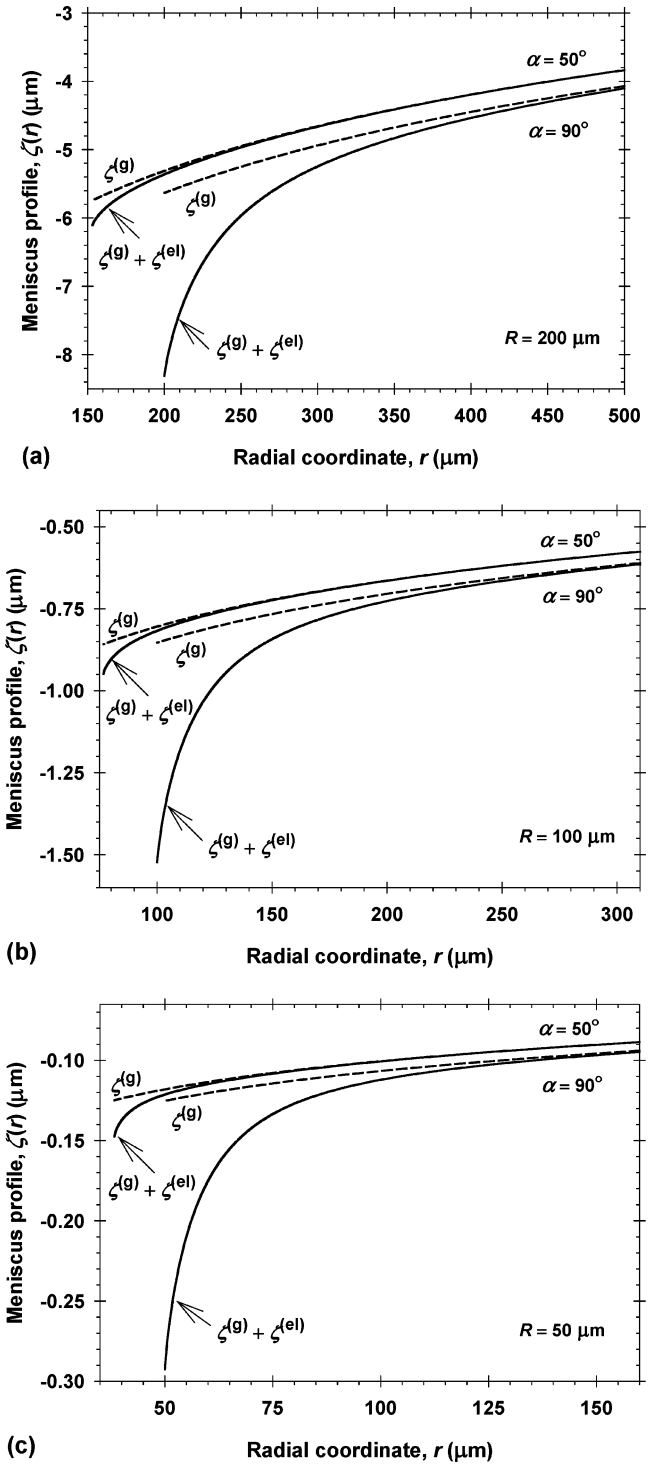


**Figure 6.** Comparison of the purely gravitational deformation, $\zeta^{(g)}$, with the total deformation, $\zeta^{(g)} + \zeta^{(el)}$, for two angles $\alpha = 50$ and 90° and for three particle radii (a) $R = 200$, (b) 100, and (c) 50 $\mu$m. $\zeta^{(g)}(r)$ and $\zeta^{(el)}(r)$ are calculated by means of eqs 2.1 and 5.22, respectively.

Equation 5.24 indicates that $\zeta^{(el)} \propto {x_1}^4$ at long distances. For this reason, it is convenient to plot $\zeta^{(el)}$ versus ${x_1}^4$ when processing experimental data (section 7). A useful parameter is the area below the curve $\zeta^{(el)}({x_1}^4)$

$$S_4 = -\int_0^1 \zeta^{(el)}(y)\, dy \qquad (6.4)$$

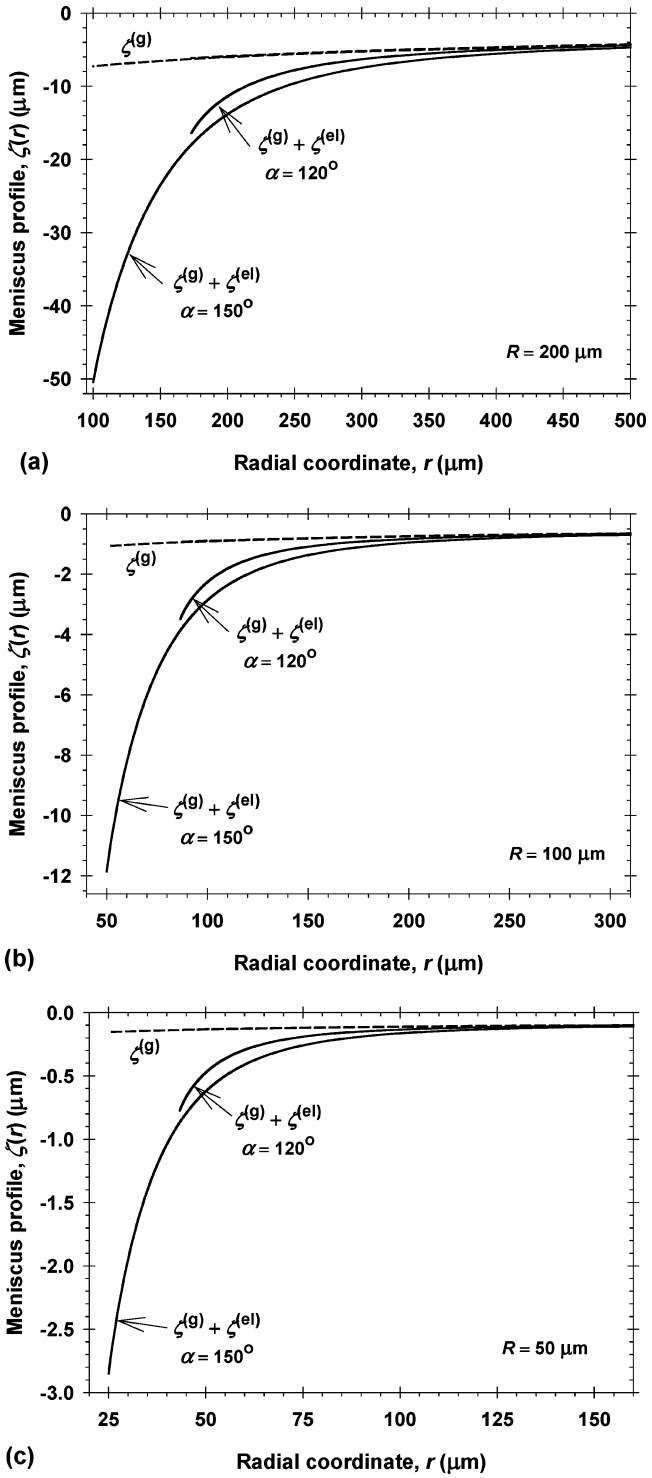


**Figure 7.** Comparison of the purely gravitational deformation, $\zeta^{(g)}$, with the total deformation, $\zeta^{(g)} + \zeta^{(el)}$, for two angles $\alpha = 120$ and 150° and for three particle radii (a) $R = 200$, (b) 100, and (c) 50 $\mu$m. $\zeta^{(g)}(r)$ and $\zeta^{(el)}(r)$ are calculated by means of eqs 2.1 and 5.22. The $\zeta^{(g)}(r)$ curves for the two $\alpha$'s practically coincide.

where $y \equiv x_1^4$. To eliminate the surface charge density, the following dimensionless ratio, $s$, is defined:

$$s \equiv \frac{h_c^{(el)}}{S_4} = \frac{-H_c^{(el)}}{\int_0^1 Z^{(el)}(y)\, dy} \tag{6.5}$$

In general, $s = s(\theta, \epsilon_{pn})$. For practical applications, it is more convenient to invert the latter dependence: $\theta = \theta(s, \epsilon_{pn})$; see

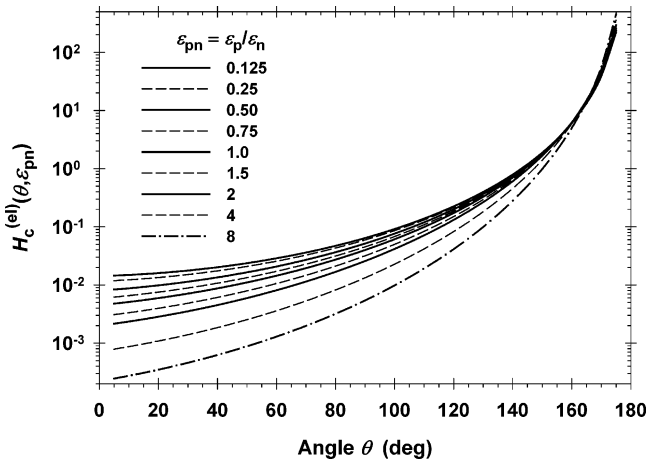


**Figure 8.** Dimensionless depth of the electric-field-induced concavity, $H_c^{(el)}$, plotted vs the contact angle $\theta$ for various values of $\epsilon_{pn}$. $H_c^{(el)}$ is calculated by means of eqs 6.2 and 6.3.

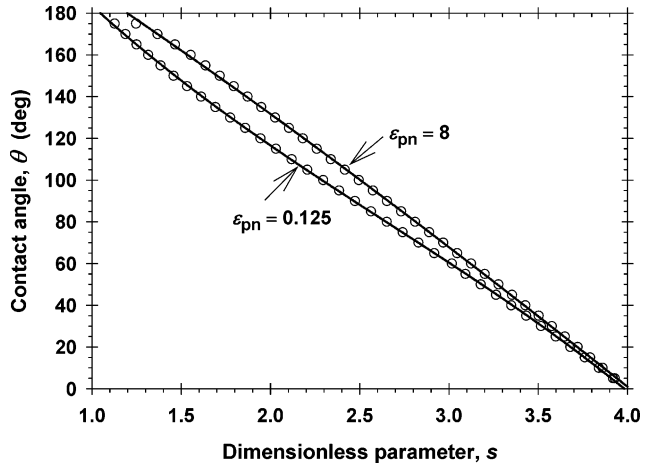


**Figure 9.** Plot of the contact angle $\theta$ vs the dimensionless parameter $s$ (eq 6.5) for two values of $\epsilon_{pn} = \epsilon_p/\epsilon_n$. The circles are computed values, whereas the lines are calculated by means of eq 6.6 and Table 1. From the experimental data, one obtains $s$ (eq 7.13), and then from the present plot, one determines the respective $\theta$.

Figure 9. For a given value of $s$, Figure 9 enables one to determine the corresponding value of the contact angle, $\theta$. For this reason, it is important that the dependence $\theta(s)$ is single-valued (Figure 9). The value of $\theta$ corresponding to a given $s$ can be determined more accurately from the equation

$$\theta = B_0 + B_1 s + B_2 s^2 + B_3 s^3 \tag{6.6}$$

where the coefficients $B_0$, $B_1$, $B_2$, and $B_3$ are given in Table 1 for various values of $\epsilon_{pn}$. For intermediate values of $\epsilon_{pn}$, the coefficients $B_0$, ..., $B_3$ could be determined by linear interpolation. The accuracy of the computation of $\theta$ by eq 6.6 and Table 1 is better than 1%.

## 7. Comparison of Theory and Experiment

The comparison of theory and experiment allows one to determine the parameters of the system and further to quantify the electric field distribution and the interactions between adsorbed particles. It is important to determine in situ the electric charge density at the particle−nonpolar fluid boundary, $\sigma_{pn}$. However, both experiment and theory have limitations that could be overcome by iteration steps, as described below. The goniometric measurements of the contact angle $\theta$ (section 7.1) give systematically smaller values of $\theta$ (denoted $\theta^{(1)}$) because the

**Table 1. Coefficients $B_0$−$B_3$ in Equation 6.6 for Various $\epsilon_{pn}$ Values**

| | $\epsilon_{pn} = \epsilon_p/\epsilon_n$ | | | | | | | | |
|---|---|---|---|---|---|---|---|---|---|
| $B_k$ | 0.125 | 0.250 | 0.500 | 0.750 | 1.00 | 1.50 | 2.00 | 4.00 | 8.00 |
| $B_0$ | 277.68 | 275.19 | 271.45 | 268.16 | 265.25 | 260.42 | 256.65 | 248.14 | 245.75 |
| $B_1$ | −113.05 | −109.22 | −103.36 | −98.079 | −93.334 | −85.228 | −78.636 | −62.061 | −51.319 |
| $B_2$ | 21.679 | 20.290 | 18.234 | 16.314 | 14.545 | 11.439 | 8.8385 | 1.9609 | −3.2356 |
| $B_3$ | −2.7119 | −2.5627 | −2.3531 | −2.1491 | −1.9558 | −1.6066 | −1.3064 | −0.48139 | 0.19163 |

**Table 2. Data for Silanized Glass Spheres at the Tetradecane−Water Interface[a]**

| $R$ ($\mu$m) | $r_c$ ($\mu$m) | $F^{(g)}$ ($\mu$N) | α (deg) | $\theta^{(1)}$ (deg) | $\theta^{(e)}$ (deg) | $\theta^{(2)}$ (deg) | $\sigma_{pn}^{(1)}$ ($\mu$C/m$^2$) | $\sigma_{pn}^{(2)}$ ($\mu$C/m$^2$) |
|---|---|---|---|---|---|---|---|---|
| 240.6 | 236.1 | 1.014 | 101.2 | 113.7 | 117.3 | 120.0 | 55.82 | 67.94 |
| 210.2 | 199.8 | 0.6836 | 108.1 | 120.8 | 125.3 | 128.7 | 56.57 | 70.48 |
| 214.4 | 203.1 | 0.7265 | 108.7 | 122.5 | 128.2 | 131.5 | 58.22 | 70.22 |
| 231.0 | 223.3 | 0.9024 | 104.8 | 117.9 | 122.8 | 124.9 | 55.70 | 68.32 |
| 200.6 | 181.3 | 0.6000 | 115.3 | 130.2 | 135.3 | 139.0 | 56.83 | 69.21 |
| 263.2 | 253.1 | 1.338 | 105.9 | 122.6 | 125.9 | 134.6 | 58.92 | 74.87 |

[a] Note that $\theta^{(1)}$ and $\sigma_{pn}^{(1)}$ are determined goniometrically (section 7.1), whereas $\theta^{(2)}$ and $\sigma_{pn}^{(2)}$ are obtained by processing data for the meniscus profile (section 7.3).

curvature of the oil−water interface increases in close proximity to the contact line, which is not accessible to optical observations (section 7.3). A more accurate value of $\theta$ (denoted $\theta^{(2)}$) could be obtained if data for the meniscus profile, such as those in Figure 3, are processed by means of the theory of the electric field distribution (sections 7.2−7.4).

**7.1. Processing Data of Goniometric Measurements.** From the side-view photographs, such as Figure 2, one can determine the radii of the particle and the contact line, $R$ and $r_c$, and then (Figure 1)

$$\alpha = \arcsin\left(\frac{r_c}{R}\right) \tag{7.1}$$

Supposedly, the particle is spherical. (When applying eq 7.1, one should take into account whether the angle α is acute or obtuse.) Furthermore, $\theta^{(1)}$ can be measured goniometrically from the photograph as the angle subtended at the contact line between the particle−water and water−nonpolar fluid interfaces. Next, one calculates $\psi_c^{(1)} = \theta^{(1)} - \alpha$.

Alternatively, $\psi_c^{(1)}$ can be measured goniometrically from the photograph as the angle subtended at the contact line between the water−nonpolar fluid interface and the horizontal plane. In our experiments (ref 37), $\psi_c^{(1)}$ was measured from the left- and right-hand-side profiles (Figure 2), and then the mean arithmetic $\psi_c^{(1)}$ was calculated. Thus, an error from the inaccurate determination of the position of the horizontal plane is avoided. Next, one calculates

$$\theta^{(1)} = \alpha + \psi_c^{(1)} \tag{7.2}$$

In general, the angle $\psi_c$ is related to the total normal force exerted on the particle, $F = F^{(el)} + F^{(g)}$, by means of eq 1.2. The gravitational force $F^{(g)}$ can be calculated by means of eq 5.3 (Table 2), whereas the electrodipping force, $F^{(el)}$, is determined by the following expression:[37,43]

$$F^{(el)} = \frac{4\pi}{\epsilon_n}\sigma_{pn}{}^2 R^2(1 - \cos\alpha)\, f(\theta, \epsilon_{pn}) \tag{7.3a}$$

Here, the multiplier $2\pi R^2(1 - \cos\alpha)$ represents the area of the particle−nonpolar fluid boundary, whereas the dimensionless force coefficient $f$, which is independent of $R$ and $\sigma_{pn}$, is related to the electrostatic interactions across the wedge-shaped region near the contact line, which is characterized by the contact angle $\theta$; see section 3.4. One could accurately calculate $f(\theta, \epsilon_{pn})$ by means of the relation

$$f(\theta, \epsilon_{pn}) = \frac{f_R(\theta, \epsilon_{pn})}{1 - \cos\theta} \tag{7.3b}$$

where the function $f_R(\theta, \epsilon_{pn})$ is tabulated in Table 3 of ref 43. (The procedure for calculating $f(\theta, \epsilon_{pn})$ based on Table 4 in ref 37 is not very accurate, so it is preferable to use Table 3 in ref 43.)

Because $F^{(el)} + F^{(g)} = 2\pi r_c\gamma \sin\psi_c$, from eq 7.3a we derive

$$\Gamma_{pn}{}^2 \equiv \frac{\sigma_{pn}{}^2}{e^2} = \frac{(2\pi r_c\gamma \sin\psi_c - F^{(g)})\epsilon_n}{4\pi e^2 R^2(1 - \cos\alpha)\, f(\theta, \epsilon_{pn})} \tag{7.4}$$

To obtain the surface charge density $\Gamma_{pn}$ in cm$^{-2}$, one has to substitute $e = 4.803 \times 10^{-10}$ (CGS units) into the right-hand side of eq 7.4.

Values $\theta^{(1)}$ and $\sigma_{pn}^{(1)}$ in Table 2 are calculated from eqs 7.2 and 7.4, respectively, where the goniometrically determined value of $\psi_c$ is substituted, along with the value of α from eq 7.1. Thus, for the particle in Figure 3 (the first row of Table 2) we have $\theta^{(1)} = 113.7°$ and $f(\theta^{(1)}, \epsilon_{pn}) = 1.323$, which gives $\sigma_{pn}^{(1)} = 55.82$ $\mu$C/m$^2$. This is the simplest way to determine the contact angle and the surface charge density.[37] However, $\theta^{(1)}$ and $\sigma_{pn}^{(1)}$ could be affected by an inaccuracy in the goniometric measurement of $\psi_c^{(1)}$; see section 7.3. For this reason, a more accurate method is presented below. Two alternative procedures for data processing are described in section 7.2 and in the Supporting Information.

**7.2. Procedure for Processing Meniscus-Profile Data.** Here, it is convenient to fix the zero of the $z$ axis at the level of the contact line, as in Figure 3. For this choice of the coordinate origin, the meniscus profile is

$$z(r) = h_c + \zeta(r) \tag{7.5}$$

where $\zeta(r)$ is the theoretical profile that satisfies the boundary conditions $\zeta(\infty) = 0$ and $\zeta(r_c) = -h_c$. As established in section 5, for small particles ($(qr_c)^2 \ll 1$), the meniscus profile can be expressed as a sum of purely electric and gravitational deformations:

$$z(r) = z^{(el)}(r) + z^{(g)}(r) \tag{7.6}$$

Here, we presume that experimental data points $(r, z)$ for a profile, such as those in Figure 3, are available. The procedure for data acquisition is described in section 2. The other input parameters are $r_c$, $\gamma$, $\epsilon_n$, $\epsilon_{pn}$, and $F^{(g)}$, the latter determined from eq 5.3. We will use the data in Figure 3 as a worked example. The procedure is as follows:

(1) For each experimental point $(r_i, z_i)$, we calculate $z^{(g)}(r_i)$ from the equation

$$z^{(g)}(r_i) = \frac{F^{(g)}}{2\pi\gamma} \ln\left(\frac{r_i}{r_c}\right) \tag{7.7}$$

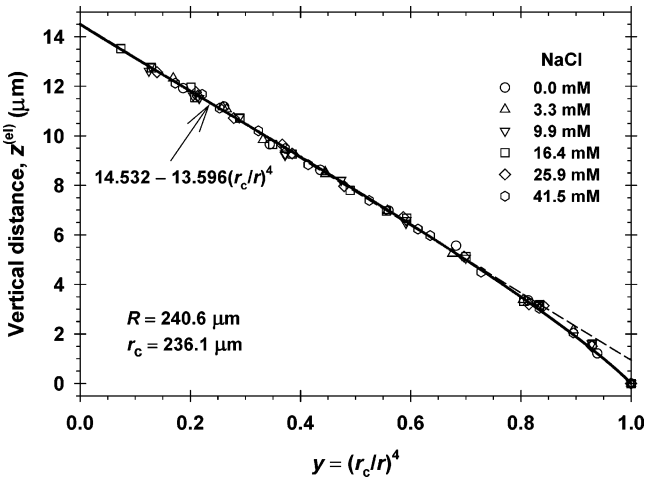


**Figure 10.** Plot of the electric interfacial deformation $z^{(el)}$ vs $y = (r_c/r)^4$ for the data in Figure 3. The solid line is a fit via cubic parabola. The dashed line is a fit via linear regression of the data for $0 < y < 0.75$; the equation of the regression is shown.

which follows from eq 5.1 and the boundary condition $z(r_c) = 0$. For the investigated particles, the values of $F^{(g)}$ are given in Table 2. Furthermore, in view of eq 7.6 we determine the electric contribution to the experimental meniscus profile:

$$z_i^{(el)} = z_i - z^{(g)}(r_i) \tag{7.8}$$

Next, we plot $z_i^{(el)}$ versus $(r_c/r_i)^4$; see Figure 10.

(2) The data for $z_i^{(el)}$ versus $y \equiv (r_c/r_i)^4$ are interpolated by a cubic parabola. In Figure 10, the best fit (the solid line) is

$$z^{(el)} = 14.532 - 16.149y + 9.628y^2 - 8.011y^3 \tag{7.9}$$

(3) The area $A_4$ below the curve $z^{(el)}(y)$ is calculated:

$$A_4 = \int_0^1 z^{(el)}(y)\,dy \tag{7.10}$$

For the curve in Figure 10, from eq 7.9 we obtain

$$A_4 = 14.532 - \frac{16.149}{2} + \frac{9.628}{3} - \frac{8.011}{4} = 7.644 \tag{7.11}$$

Next, we calculate the dimensionless ratio, $u$:

$$u \equiv \frac{z^{(el)}(y=0)}{A_4} = \frac{14.532}{7.644} = 1.901 \tag{7.12}$$

The parameter $s$ (section 6.2) is

$$s \equiv \frac{u}{u-1} = 2.110 \tag{7.13}$$

(4) We determine the parameters $B_0(\epsilon_{pn})$, $B_1(\epsilon_{pn})$, $B_2(\epsilon_{pn})$, and $B_3(\epsilon_{pn})$ from Table 1 by linear interpolation:

$$f(x) = f(x_1) + \frac{f(x_2) - f(x_1)}{x_2 - x_1}(x - x_1) \tag{7.14}$$

For the data in Figure 3, we have $\epsilon_{pn} = 1.946$, and then with the help of eq 7.14 from Table 1 we find

$$B_0 = 257.06 \qquad B_1 = -79.348 \qquad B_2 = 9.1194 \qquad B_3 = -1.3388 \tag{7.15}$$

Substituting $s$ from eq 7.13 and $B_0 - B_3$ from eq 7.15 into eq 6.6, we calculate the contact angle $\theta \equiv \theta^{(e)} = 117.3°$. This procedure is applicable for every $\theta \in (0°, 180°)$. The value of $\theta$ determined here is denoted $\theta^{(e)}$ to distinguish it from the values $\theta^{(1)}$ and $\theta^{(2)}$ obtained in sections 7.1 and 7.3; see Table 2 and the discussion in section 7.3. For contact angles $5° \le \theta \le 120°$, one can use a simpler procedure, which is described at the end of the Supporting Information.

**7.3. Determination of the Surface Charge Density.** Having obtained $\theta = \theta^{(e)}$ (section 7.2) and knowing $\epsilon_{pn}$, we determine $H_c^{(el)}(\theta^{(e)}, \epsilon_{pn})$ from Table D in the Supporting Information. For this purpose, one can use the four-point interpolation formula

$$f(x,y) = \frac{(x-x_2)(y-y_2)}{(x_1-x_2)(y_1-y_2)}f(x_1,y_1) + \frac{(x-x_2)(y-y_1)}{(x_1-x_2)(y_2-y_1)} \times f(x_1,y_2) + \frac{(x-x_1)(y-y_2)}{(x_2-x_1)(y_1-y_2)}f(x_2,y_1) + \frac{(x-x_1)(y-y_1)}{(x_2-x_1)(y_2-y_1)} \times f(x_2,y_2) \tag{7.16}$$

Thus, for $\theta = 117.3°$ and $\epsilon_{pn} = 1.946$, we obtain

$$\ln H_c^{(el)} = -2.1864 \text{ and } H_c^{(el)} = 0.11233 \tag{7.17}$$

Next, we calculate the theoretical meniscus profile with the help of eqs 3.8, 6.3, and 7.5−7.7

$$z(r) = \frac{F^{(g)}}{2\pi\gamma}\ln\left(\frac{r}{r_c}\right) + \frac{h_c^{(el)}}{H_c^{(el)}}\hat{Z}^{(el)}(x_1) \tag{7.18}$$

where the zero on the $z$ axis is chosen such that $z(r_c) = 0$. Keeping in mind that $h_c^{(el)} = z^{(el)}$ $(y = 0)$, we determine the scaling factor $h_c^{(el)}/H_c^{(el)}$ in eq 7.18. For the data in Figure 3, we have $h_c^{(el)} = z^{(el)}$ $(y = 0) = 14.532$ $\mu$m (eq 7.9), and then $h_c^{(el)}/H_c^{(el)} = 129.37$ $\mu$m (eq 7.17). Furthermore, using Tables A, B, and C in the Supporting Information, with the help of eq 7.16 we determined coefficients $a$, $b$, and $c$ in eq 3.8b:

$$a = 9.012 \qquad b = -7.207 \qquad c = 0.08252 \tag{7.19}$$

Now all parameters in eqs 3.8b and 7.18 are known, and we can calculate the theoretical meniscus profile; see the solid line in Figure 3. This profile can be considered to be the best fit of the experimental data. (The procedure in section 7.2 includes a fit by cubic parabola.) As seen in Figure 3 and in section 7.4, the theoretical profile is in excellent agreement with the experimental data.

Next, by differentiation of eq 7.18 along with eq 3.8b, we obtain the meniscus slope angle at the contact line:

$$\tan\psi_c^{(2)} = \frac{F^{(g)}}{2\pi\gamma r_c} + \frac{dz^{(el)}}{dr}\Big|_{r=r_c} \tag{7.20}$$

$$\frac{dz^{(el)}}{dr}\Big|_{r=r_c} = \frac{2h_c^{(el)}}{(a+b)r_c H_c^{(el)}}[(4a+3b)H_c^{(el)} - 1 - c] \tag{7.21}$$

For the considered illustrative example (the first row of Table 2), we compute $(dz^{(el)}/dr)|_{r=r_c} = 0.3271$, which, after substitution into eq 7.20, gives $\psi_c^{(2)} = 18.8°$. The corresponding value of the contact angle is $\theta^{(2)} \equiv \alpha + \psi_c^{(2)} = 120.0°$.

Finally, after substituting $\theta = \theta^{(e)}$ and $\psi_c = \psi_c^{(2)}$ into eq 7.4, we calculate the surface charge density. For the considered example, we have $f(\theta^{(e)}, \epsilon_{pn}) = 1.360$, which gives $\sigma_{pn}^{(2)} = 67.9$ $\mu$C/m$^2$.

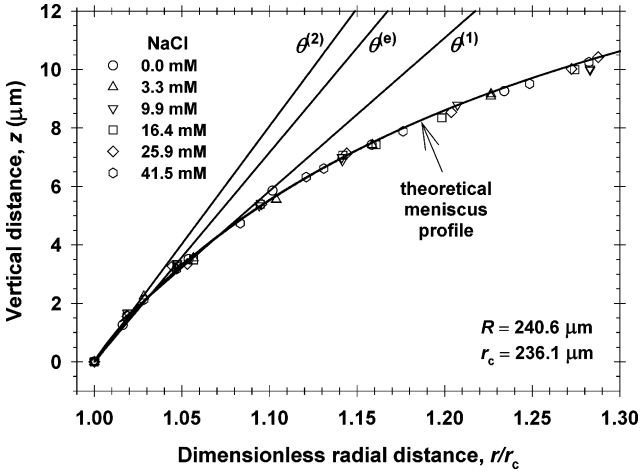


**Figure 11.** Data from Figure 3 on an enlarged scale. The solid line is the theoretical profile. The three tangents correspond to three values of the contact angle: the goniometric value $\theta^{(1)}$ measured from the photograph, the effective value $\theta^{(e)}$ obtained from the fit of the data in section 7.2, and $\theta^{(2)} = \alpha + \psi_c^{(2)}$ calculated from the theoretical slope at the contact line, $\psi_c^{(2)}$ (eqs 7.20−7.21).

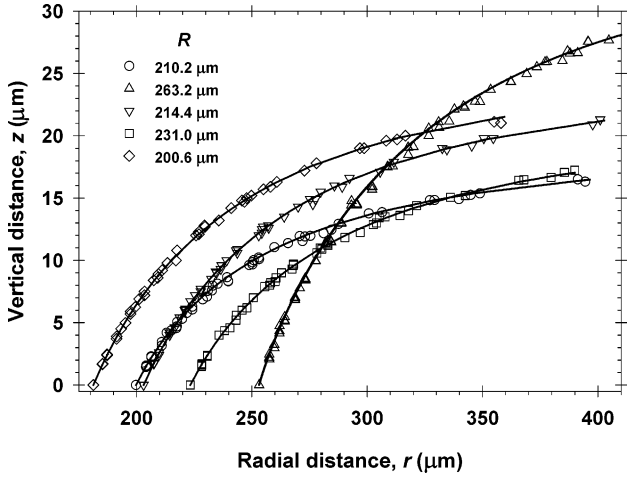


**Figure 12.** Meniscus shape, $z(r)$, around five different silanized glass particles at the water−tetradecane interface. The symbols are digitized points on the meniscus profile taken from photomicrographs such as in Figure 2. The solid lines are the best fits via the theoretical profile.

In Table 2, the values of $\theta^{(2)} \equiv \alpha + \psi_c^{(2)}$ are systematically greater than those of $\theta^{(e)}$ (the latter have been determined as described in section 7.2). In Figure 11, the data from Figure 3 are presented on an enlarged scale. One sees that the slope of the theoretical curve increases in a narrow zone (of width ∼2% of $r_c$) near the contact line; this zone is not seen well in the photomicrographs, such as in Figure 2. Correspondingly, the actual slope angle at the contact line, $\psi_c^{(2)}$, is greater than the goniometrically determined $\psi_c^{(1)}$. Because the solid line in Figure 11 represents the best theoretical fit of the experimental data, we should expect that this curve adequately describes the meniscus shape near the contact line. Correspondingly, $\theta^{(2)}$ and $\psi_c^{(2)}$ are more reliable values of the contact and slope angles, in comparison with $\theta^{(1)}$ and $\psi_c^{(1)}$.

The origin of the difference between $\theta^{(e)}$ and $\theta^{(2)}$ is related to the simplifying assumption that $\theta \approx \alpha$ when solving the electrostatic boundary problem.[37,43] As discussed in section 3.4, $\theta^{(e)}$, which is determined by a comparison of theory and experiment (section 7.2), characterizes the effective angle ($\pi - \theta^{(e)}$) of the wedge-shaped region filled by the nonpolar fluid near the contact line (Figure 1). We could consider $\theta^{(e)}$ to be an auxiliary parameter, which allows one to compute the theoretical profile $z(r)$ (that agrees very well with the experimental points, see Figures 3, 11, and 12), and to estimate the real slope, $\psi_c^{(2)}$, at the contact line. After substituting $\theta = \theta^{(e)}$ and $\psi_c = \psi_c^{(2)}$ into eq 7.4, we obtain a value of the surface charge density, $\sigma_{pn}^{(2)}$, that is more accurate than the value $\sigma_{pn}^{(1)}$ determined from the goniometric data (section 7.1).

The values of $\sigma_{pn}^{(2)}$ obtained for different particles here and listed in Table 2 are close to the values of $\sigma_{pn}$ reported in our previous article,[37] all of them about 70 $\mu$C/m$^2$. In ref 37, the goniometric method was used to determine $\psi_c$, whereas numerical integration with a finite step was applied to calculate the force coefficient $f(\theta, \epsilon_{pn})$. It turns out that the applied experimental and numerical methods give $\psi_c$ and $f$ values that smaller than their real values; for more information about $f$, see the discussion after eq 5.21 in ref 43. Because $\psi_c$ and $f$ enter the numerator and denominator of eq 7.4, respectively, it happens that the errors in the latter two parameters affect the calculated $\sigma_{pn}$ in opposite directions and cancel each other. This explains the similar values of $\sigma_{pn}$ obtained in ref 37 and in the present article (Table 2).

However, the values of $\sigma_{pn}^{(1)}$ in Table 2 are obtained from the goniometric $\psi_c^{(1)}$ but using the accurate values of $f(\theta, \epsilon_{pn})$ from eq 7.3b. Note that in the considered range of angles we have $f(\theta, \epsilon_{pn}) \approx f(\alpha, \epsilon_{pn})$ (i.e., $f$ is insensitive to the value of the angle). For this reason, the systematic difference between $\sigma_{pn}^{(1)}$ and $\sigma_{pn}^{(2)}$ in Table 2 is entirely due to the fact that $\psi_c^{(1)} < \psi_c^{(2)}$; see eq 7.4.

In general, the procedure for obtaining the surface charge density, $\sigma_{pn}^{(2)}$, developed in the present article is more reliable than that in ref 37 because the used tabulated functions (see the Supporting Information) are obtained with the help of the exact analytical asymptotics of the electric field at $r \to r_c$, derived in ref 43. In addition, here the meniscus slope angle, $\psi_c^{(2)}$, is determined from the theoretical fit of experimental data for the interfacial profile (Figure 11) rather than by goniometry of video frames (Figure 2).

**7.4. Comparison of Theory and Experiment for Various Particles.** To illustrate the procedure for data processing, in sections 7.1−7.3 we considered the experimental results for a single particle (Figure 3), as a worked example. Experimental results for five other particles are shown in Figure 12, and the determined parameter values are listed in Table 2. As in Figure 3, photographs of the same particle, taken at different NaCl concentrations, have been processed. Because there is no effect of the NaCl on the meniscus shape (which provides evidence for predominant electrostatic interactions across the *nonaqueous* phases), the full set of data for a given particle is fitted with a single theoretical curve.

The theoretical curves are drawn with the help of the procedure described in sections 7.2 and 7.3. As seen in Figure 12, there is excellent agreement between theory and experiment. The obtained values of the determined parameters $\theta^{(e)}$, $\theta^{(2)}$, and $\sigma_{pn}^{(2)}$ are listed in Table 2. One sees that $\theta^{(2)}$ slightly varies from particle to particle, whereas the surface charge density, $\sigma_{pn}^{(2)}$, is almost the same. Its average value is $\sigma_{pn}^{(2)} = 70.2 \pm 1.0$ $\mu$C/m$^2$. A similar value, 80 $\mu$C/m$^2$, was obtained[23] from the data of Philipse and Vrij[52] for zeta potentials of silanized silica particles in toluene−ethanol mixtures. Note that 80 $\mu$C/m$^2$ is a rather low surface charge density: it is equivalent to 2000 nm$^2$ per charge. Nevertheless, our computations show that even such small surface

(52) Philipse, A. P.; Vrij, A. *J. Colloid Interface Sci.* **1989**, *128*, 121−136.

charge is able to cause the observed interfacial deformations owing to the low dielectric constant of the nonpolar fluid; see also ref 22. Even lower surface charge, $1-20\ \mu C/m^2$, was estimated[23] from the data of Labib and Williams[53] for glass particles in several pure organic solvents.

The experimental data in Figures 3 and 12 and their theoretical fits show that for all investigated particles the electric field creates a strong deformation of the oil−water interface in the region from $r = r_c$ to $r = 3-4(r_c)$. In comparison with the *long*-range deformation created by the gravitational force, the electric field creates a deformation of *medium* range. For the investigated particles, the amplitude of the electric deformation is much greater than the amplitude of the gravitational one.

## 8. Summary and Conclusions

The present article is a continuation of our previous study,[37] where the main attention has been focused on the electrodipping force acting on a charged dielectric particle, which is attached to the water−nonpolar fluid (air, oil) boundary; see Figure 1. In a subsequent study,[43] we obtained analytical solution describing the electric field created by the particle. As a next step, here we consider in more detail the problem of the calculation of the shape of the fluid interface around the particle. The electric field created by charges at the particle−nonpolar fluid boundary could give rise to a considerable deformation of the surrounding fluid interface.

We digitized the coordinates of points from the meniscus profile around silanized glass particles attached to the water−tetradecane interface (section 2; Figures 3 and 12). The experimental shape of the oil−water interface is independent of the concentration of NaCl in the aqueous phase, which confirms that the electric field in the nonaqueous phases dominates the electrostatic interactions in the investigated system. The theoretical meniscus profile, $\zeta(r)$, can be computed in three different ways, which give numerically coincident results. First, $\zeta(r)$ can be calculated by the numerical solution of the electrostatic boundary problem[37] (section 3.1). Second, $\zeta(r)$ can be computed from the analytical solution of the problem, based on the Mehler−Fock integral transform[43] (section 3.2). Third, $\zeta(r)$ can be calculated by means of an interpolation formula, eq 3.8, whose coefficients are determined by fits of the numerical data and are tabulated in the Supporting Information for this article.

Furthermore, in section 5 it is proven that for sufficiently small particles ($(qr_c)^2 \ll 1$) the meniscus profile can be expressed as a superposition of pure electric and gravitational deformations, $\zeta(r) = \zeta^{(el)}(r) + \zeta^{(g)}(r)$. The latter fact considerably simplifies the calculations. The comparison of the gravitational and electric deformations (Figures 6 and 7) indicates that the range of the electric deformation markedly depends on the contact angle: thus, for angles of 50 and 150° the range is, respectively, about 1.5 and 5 contact-line radii (section 6.1). Theoretical expressions and numerical results are also obtained for the depth of the concavity, $h_c$, produced by the particle, which strongly depends on the contact angle (section 6.2 and Figure 8).

Special attention is paid to the comparison of theory and experiment, which is considered in section 7. On the basis of the obtained theoretical expressions and numerical results, a relatively simple procedure for processing experimental data is developed, which is reduced to fitting the data for the meniscus profile via cubic parabola (section 7.2) or linear regression (Supporting Information). Next, the theoretical interfacial profile is reproduced by eq 7.18, and the meniscus slope at the contact line is accurately determined via differentiation of the theoretical profile. This allows one to obtain values of the contact angle and surface charge density, $\theta^{(2)}$ and $\sigma_{pn}^{(2)}$ (section 7.3), which are more accurate than those determined by the goniometric method (section 7.1). For all investigated particles, excellent agreement between theory and experiment is achieved (Figures 3 and 12).

The theoretical analysis (sections 4 and 6) and the experimental results (Figures 3 and 12) lead to the conclusion that the electric-field-induced deformation of the fluid interface has a medium range, from 1.5 to 5 contact-line radii, depending on the contact angle. At larger distances, the meniscus profile is governed solely by the gravitational force. However, for $r < 5r_c$ the electric field creates a concavity (dimple) of significant depth in the fluid interface around the particle. For the experimentally investigated particles, the electric interfacial deformation has shorter range but greater amplitude than the gravitational deformation. The results could be useful for a better understanding of the lateral capillary forces between particles at emulsion interfaces, which lead to packing of the particle adsorption layer and the stabilization of Pickering emulsions.

**Acknowledgment.** This work was supported by the program "Cooperation and Networking for Excellence" (CONEX), financed by the Austrian Ministry of Education, Science and Culture. We thank Dr. Tommy S. Horozov for the helpful discussions.

**Supporting Information Available:** Functions $\ln(a(\theta, \epsilon_{pn}), b(\theta, \epsilon_{pn}), c(\theta, \epsilon_{pn}), \ln(H_c^{(el)}(\theta, \epsilon_{pn}),$ and $\ln(Q(\theta, \epsilon_{pn})$ for various values of $\theta$ and $\epsilon_{pn}$. Second procedure for processing meniscus-profile data. This material is available free of charge via the Internet at http://pubs.acs.org.

LA052749Z

(53) Labib, M. E.; Williams, R. *J. Colloid Interface Sci.* **1987**, *115*, 330−338.

## Supporting Information

**For the Paper: Shape of the Capillary Meniscus around an Electrically Charged Particle at a Fluid Interface: Comparison of Theory and Experiment**

**Authors: *K. D. Danov, P. A. Kralchevsky, and M. P. Boneva***

The dimensionless meniscus profile is described by the equation:

$$\hat{Z}^{(\mathrm{el})}(x_1) = \frac{H_{\mathrm{c}}^{(\mathrm{el})}}{a+bx_1^2}\left[a(1-x_1^8)+bx_1^2(1-x_1^6)\right] - x_1^4(1-x_1^2)\frac{1+cx_1^2}{a+bx_1^2}$$

see eq 3.8 in the main paper. Here $a$, $b$, $c$, and $H_{\mathrm{c}}^{(\mathrm{el})}$ are parameters (independent of $x_1 \equiv r_{\mathrm{c}}/r$), which depend on the particle contact angle, $\theta$, and on the dielectric constant ratio, $\varepsilon_{\mathrm{pn}} = \varepsilon_{\mathrm{p}}/\varepsilon_{\mathrm{n}}$. These dependencies are tabulated in Tables A, B, C and D, which are to be used along with the four-point interpolation formula, eq 7.16.

**Table A.** Function $\ln[a(\theta,\varepsilon_{\mathrm{pn}})]$ for various $\theta$ and $\varepsilon_{\mathrm{pn}}$.

| | $\varepsilon_{\mathrm{pn}} = \varepsilon_{\mathrm{p}}/\varepsilon_{\mathrm{n}}$ | | | | | | | | |
|---|---|---|---|---|---|---|---|---|---|
| $\theta$ | 0.125 | 0.250 | 0.500 | 0.750 | 1.00 | 1.50 | 2.00 | 4.00 | 8.00 |
| 5 | 6.058 | 6.260 | 6.611 | 6.909 | 7.169 | 7.605 | 7.963 | 8.970 | 10.14 |
| 10 | 5.992 | 6.185 | 6.522 | 6.811 | 7.064 | 7.489 | 7.840 | 8.833 | 9.990 |
| 15 | 5.916 | 6.101 | 6.426 | 6.705 | 6.950 | 7.365 | 7.708 | 8.687 | 9.833 |
| 20 | 5.832 | 6.008 | 6.320 | 6.590 | 6.827 | 7.232 | 7.568 | 8.531 | 9.667 |
| 25 | 5.738 | 5.906 | 6.206 | 6.466 | 6.696 | 7.090 | 7.418 | 8.366 | 9.490 |
| 30 | 5.635 | 5.795 | 6.082 | 6.333 | 6.555 | 6.938 | 7.259 | 8.190 | 9.303 |
| 35 | 5.521 | 5.674 | 5.948 | 6.190 | 6.405 | 6.777 | 7.090 | 8.005 | 9.105 |
| 40 | 5.397 | 5.542 | 5.805 | 6.037 | 6.245 | 6.605 | 6.911 | 7.808 | 8.896 |
| 45 | 5.262 | 5.400 | 5.651 | 5.874 | 6.074 | 6.423 | 6.721 | 7.600 | 8.674 |
| 50 | 5.115 | 5.247 | 5.486 | 5.700 | 5.893 | 6.230 | 6.519 | 7.380 | 8.440 |
| 55 | 4.957 | 5.081 | 5.309 | 5.514 | 5.699 | 6.026 | 6.306 | 7.147 | 8.193 |
| 60 | 4.785 | 4.903 | 5.120 | 5.316 | 5.494 | 5.809 | 6.080 | 6.902 | 7.931 |
| 65 | 4.600 | 4.712 | 4.918 | 5.105 | 5.275 | 5.578 | 5.841 | 6.642 | 7.655 |
| 70 | 4.401 | 4.506 | 4.702 | 4.880 | 5.043 | 5.334 | 5.588 | 6.367 | 7.363 |
| 75 | 4.186 | 4.286 | 4.471 | 4.640 | 4.796 | 5.075 | 5.319 | 6.077 | 7.054 |
| 80 | 3.955 | 4.048 | 4.223 | 4.384 | 4.532 | 4.799 | 5.035 | 5.769 | 6.727 |
| 85 | 3.705 | 3.793 | 3.958 | 4.110 | 4.251 | 4.506 | 4.732 | 5.443 | 6.380 |
| 90 | 3.436 | 3.519 | 3.674 | 3.818 | 3.951 | 4.194 | 4.411 | 5.097 | 6.012 |
| 95 | 3.146 | 3.223 | 3.369 | 3.504 | 3.631 | 3.862 | 4.068 | 4.729 | 5.620 |
| 100 | 2.831 | 2.903 | 3.040 | 3.167 | 3.287 | 3.506 | 3.702 | 4.337 | 5.203 |
| 105 | 2.491 | 2.558 | 2.686 | 2.805 | 2.918 | 3.124 | 3.311 | 3.918 | 4.758 |
| 110 | 2.120 | 2.183 | 2.302 | 2.414 | 2.520 | 2.714 | 2.891 | 3.470 | 4.282 |
| 115 | 1.717 | 1.775 | 1.886 | 1.991 | 2.089 | 2.272 | 2.439 | 2.989 | 3.771 |
| 120 | 1.274 | 1.329 | 1.432 | 1.530 | 1.622 | 1.794 | 1.950 | 2.471 | 3.221 |
| 125 | 0.7868 | 0.8373 | 0.9337 | 1.025 | 1.111 | 1.272 | 1.418 | 1.910 | 2.625 |
| 130 | 0.2465 | 0.2934 | 0.3829 | 0.4674 | 0.5475 | 0.6972 | 0.8344 | 1.297 | 1.976 |
| 135 | –0.3569 | –0.3135 | –0.2307 | –0.1525 | -0.0782 | 0.0605 | 0.1881 | 0.6198 | 1.262 |
| 140 | –1.038 | –0.9978 | –0.9212 | –0.8489 | -0.7802 | –0.6520 | –0.5339 | –0.1324 | 0.4688 |
| 145 | –1.818 | –1.781 | –1.709 | –1.642 | -1.579 | –1.461 | –1.352 | –0.9810 | –0.4224 |
| 150 | –2.730 | –2.695 | –2.627 | –2.564 | -2.505 | –2.395 | –2.295 | –1.954 | –1.440 |
| 155 | –3.832 | –3.797 | –3.730 | –3.669 | -3.612 | –3.507 | –3.413 | –3.099 | –2.627 |
| 160 | –5.254 | –5.211 | –5.135 | –5.066 | -5.005 | –4.896 | –4.801 | –4.498 | –4.065 |
| 165 | –7.528 | –7.426 | –7.261 | –7.130 | -7.023 | –6.852 | –6.719 | –6.356 | –5.913 |

**Table B.** Function $b(\theta,\varepsilon_{pn})$ for various $\theta$ and $\varepsilon_{pn}$.

| $\theta$ | $\varepsilon_{pn} = \varepsilon_p/\varepsilon_n$ | | | | | | | | |
|---|---|---|---|---|---|---|---|---|---|
| | 0.125 | 0.250 | 0.500 | 0.750 | 1.00 | 1.50 | 2.00 | 4.00 | 8.00 |
| 5 | –385.5 | –471.7 | –670.1 | –903.4 | –1171 | –1812 | –2591 | –7099 | –22789 |
| 10 | –359.3 | –435.9 | –611.3 | –816.2 | –1051 | –1608 | –2284 | –6170 | –19617 |
| 15 | –331.9 | –399.3 | –552.7 | –731.0 | –934.2 | –1415 | –1996 | –5313 | –16723 |
| 20 | –303.6 | –362.3 | –495.3 | –648.9 | –823.3 | –1234 | –1728 | –4531 | –14114 |
| 25 | –275.1 | –325.7 | –439.7 | –570.7 | –718.9 | –1066 | –1482 | –3827 | –11790 |
| 30 | –246.7 | –289.8 | –386.6 | –497.2 | –621.8 | –912.4 | –1259 | –3198 | –9743 |
| 35 | –218.8 | –255.3 | –336.5 | –428.9 | –532.4 | –772.9 | –1058 | –2645 | –7962 |
| 40 | –192.0 | –222.4 | –289.8 | –366.0 | –451.2 | –647.9 | –880.2 | –2163 | –6431 |
| 45 | –166.5 | –191.6 | –246.8 | –309.0 | –378.2 | –537.2 | –724.1 | –1749 | –5132 |
| 50 | –142.7 | –163.0 | –207.8 | –257.9 | –313.4 | –440.4 | –588.8 | –1397 | –4044 |
| 55 | –120.6 | –137.0 | –172.8 | –212.6 | –256.6 | –356.7 | –473.1 | –1102 | –3144 |
| 60 | –100.6 | –113.6 | –141.8 | –173.1 | –207.4 | –285.2 | –375.2 | –857.7 | –2411 |
| 65 | –82.72 | –92.87 | –114.8 | –139.0 | –165.4 | –225.0 | –293.7 | –658.4 | –1822 |
| 70 | –66.94 | –74.76 | –91.59 | –110.0 | –130.1 | –175.1 | –226.6 | –498.0 | –1355 |
| 75 | –53.27 | –59.21 | –71.92 | –85.76 | –100.7 | –134.2 | –172.2 | –370.9 | –992.1 |
| 80 | –41.63 | –46.08 | –55.54 | –65.77 | –76.78 | –101.2 | –128.8 | –271.7 | –713.7 |
| 85 | –31.92 | –35.21 | –42.14 | –49.57 | –57.53 | –75.06 | –94.77 | –195.7 | –504.1 |
| 90 | –23.97 | –26.36 | –31.37 | –36.68 | –42.33 | –54.69 | –68.48 | –138.3 | –349.0 |
| 95 | –17.61 | –19.33 | –22.89 | –26.62 | –30.56 | –39.08 | –48.53 | –95.79 | –236.5 |
| 100 | –12.63 | –13.85 | –16.34 | –18.91 | –21.59 | –27.34 | –33.66 | –64.85 | –156.3 |
| 105 | –8.799 | –9.664 | –11.37 | –13.09 | –14.87 | –18.64 | –22.75 | –42.74 | –100.4 |
| 110 | –5.852 | –6.461 | –7.607 | –8.735 | –9.880 | –12.28 | –14.86 | –27.22 | –62.29 |
| 115 | –3.388 | –3.869 | –4.680 | –5.422 | –6.150 | –7.635 | –9.200 | –16.54 | –36.92 |
| 120 | –0.8982 | –1.472 | –2.190 | –2.753 | –3.253 | –4.194 | –5.133 | –9.308 | –20.50 |
| 125 | 0.6153 | 0.3173 | –0.1610 | –0.6174 | –0.9753 | –1.603 | –2.179 | –4.474 | –10.16 |
| 130 | 0.8858 | 0.8218 | 0.6765 | 0.5233 | 0.3710 | 0.04676 | –0.2459 | –1.369 | –3.912 |
| 135 | 0.7451 | 0.7582 | 0.7666 | 0.7575 | 0.7365 | 0.6728 | 0.5957 | 0.2587 | –0.5593 |
| 140 | 0.5562 | 0.5769 | 0.6129 | 0.6411 | 0.6630 | 0.6925 | 0.7087 | 0.7189 | 0.7158 |
| 145 | 0.3860 | 0.4007 | 0.4277 | 0.4520 | 0.4748 | 0.5148 | 0.5491 | 0.6548 | 0.8563 |
| 150 | 0.2477 | 0.2554 | 0.2703 | 0.2845 | 0.2981 | 0.3237 | 0.3483 | 0.4354 | 0.6027 |
| 155 | 0.1443 | 0.1474 | 0.1537 | 0.1599 | 0.1662 | 0.1784 | 0.1904 | 0.2364 | 0.3256 |
| 160 | 0.07404 | 0.07487 | 0.07666 | 0.07858 | 0.08058 | 0.08474 | 0.08901 | 0.1063 | 0.1415 |
| 165 | 0.03170 | 0.03172 | 0.03184 | 0.03205 | 0.03234 | 0.03305 | 0.03391 | 0.03795 | 0.04693 |

**Table C.** Function $c(\theta,\varepsilon_{pn})$ for various $\theta$ and $\varepsilon_{pn}$.

| $\theta$ | $\varepsilon_{pn} = \varepsilon_p/\varepsilon_n$ | | | | | | | | |
|---|---|---|---|---|---|---|---|---|---|
| | 0.125 | 0.250 | 0.500 | 0.750 | 1.00 | 1.50 | 2.00 | 4.00 | 8.00 |
| 5 | 1.021 | 1.021 | 1.021 | 1.021 | 1.021 | 1.021 | 1.021 | 1.021 | 1.021 |
| 10 | 1.013 | 1.013 | 1.013 | 1.013 | 1.013 | 1.013 | 1.013 | 1.013 | 1.013 |
| 15 | 1.004 | 1.004 | 1.004 | 1.004 | 1.004 | 1.004 | 1.004 | 1.003 | 1.003 |
| 20 | 0.9937 | 0.9937 | 0.9935 | 0.9935 | 0.9934 | 0.9933 | 0.9933 | 0.9931 | 0.9931 |
| 25 | 0.9829 | 0.9827 | 0.9825 | 0.9824 | 0.9825 | 0.9824 | 0.9823 | 0.9821 | 0.9820 |
| 30 | 0.9713 | 0.9710 | 0.9707 | 0.9705 | 0.9703 | 0.9701 | 0.9699 | 0.9696 | 0.9694 |
| 35 | 0.9583 | 0.9580 | 0.9575 | 0.9571 | 0.9569 | 0.9565 | 0.9563 | 0.9558 | 0.9555 |
| 40 | 0.9440 | 0.9435 | 0.9428 | 0.9423 | 0.9420 | 0.9414 | 0.9411 | 0.9404 | 0.9400 |
| 45 | 0.9283 | 0.9276 | 0.9266 | 0.9259 | 0.9254 | 0.9247 | 0.9242 | 0.9233 | 0.9227 |
| 50 | 0.9108 | 0.9099 | 0.9085 | 0.9076 | 0.9068 | 0.9059 | 0.9052 | 0.9040 | 0.9031 |
| 55 | 0.8913 | 0.8901 | 0.8883 | 0.8870 | 0.8860 | 0.8847 | 0.8838 | 0.8821 | 0.8810 |
| 60 | 0.8695 | 0.8678 | 0.8654 | 0.8637 | 0.8624 | 0.8606 | 0.8595 | 0.8572 | 0.8562 |
| 65 | 0.8449 | 0.8428 | 0.8396 | 0.8373 | 0.8356 | 0.8333 | 0.8318 | 0.8289 | 0.8271 |
| 70 | 0.8169 | 0.8141 | 0.8099 | 0.8069 | 0.8047 | 0.8017 | 0.7998 | 0.7960 | 0.7937 |
| 75 | 0.7848 | 0.7811 | 0.7756 | 0.7717 | 0.7689 | 0.7650 | 0.7625 | 0.7578 | 0.7549 |
| 80 | 0.7476 | 0.7428 | 0.7356 | 0.7307 | 0.7270 | 0.7221 | 0.7189 | 0.7130 | 0.7094 |
| 85 | 0.7041 | 0.6978 | 0.6886 | 0.6822 | 0.6776 | 0.6714 | 0.6675 | 0.6603 | 0.6560 |
| 90 | 0.6526 | 0.6444 | 0.6325 | 0.6245 | 0.6187 | 0.6110 | 0.6063 | 0.5977 | 0.5929 |
| 95 | 0.5909 | 0.5802 | 0.5651 | 0.5551 | 0.5480 | 0.5389 | 0.5333 | 0.5237 | 0.5186 |
| 100 | 0.5164 | 0.5026 | 0.4838 | 0.4717 | 0.4634 | 0.4530 | 0.4468 | 0.4366 | 0.4317 |
| 105 | 0.4277 | 0.4100 | 0.3871 | 0.3730 | 0.3637 | 0.3524 | 0.3460 | 0.3361 | 0.3320 |
| 110 | 0.3320 | 0.3083 | 0.2796 | 0.2631 | 0.2526 | 0.2402 | 0.2335 | 0.2240 | 0.2211 |
| 115 | 0.2793 | 0.2359 | 0.1881 | 0.1627 | 0.1470 | 0.1293 | 0.1200 | 0.1075 | 0.1041 |
| 120 | 0.4516 | 0.3222 | 0.2010 | 0.1374 | 0.09915 | 0.05658 | 0.0342 | 0.0027 | –0.0086 |
| 125 | 0.7385 | 0.6074 | 0.4266 | 0.2888 | 0.2042 | 0.09913 | 0.0390 | –0.0547 | –0.0953 |
| 130 | 0.8261 | 0.7600 | 0.6351 | 0.5266 | 0.4355 | 0.2852 | 0.1856 | –0.0084 | –0.1169 |
| 135 | 0.7638 | 0.7496 | 0.7064 | 0.6526 | 0.5955 | 0.4855 | 0.3907 | 0.1528 | –0.0379 |
| 140 | 0.6573 | 0.6669 | 0.6735 | 0.6653 | 0.6473 | 0.5953 | 0.5352 | 0.3248 | 0.1155 |
| 145 | 0.5404 | 0.5613 | 0.5911 | 0.6079 | 0.6169 | 0.6144 | 0.5949 | 0.4672 | 0.2812 |
| 150 | 0.4222 | 0.4461 | 0.4859 | 0.5164 | 0.5391 | 0.5660 | 0.5786 | 0.5438 | 0.4139 |
| 155 | 0.3057 | 0.3282 | 0.3686 | 0.4031 | 0.4324 | 0.4775 | 0.5080 | 0.5485 | 0.4910 |
| 160 | 0.1931 | 0.2115 | 0.2463 | 0.2781 | 0.3072 | 0.3571 | 0.3972 | 0.4870 | 0.5151 |
| 165 | 0.08604 | 0.09911 | 0.1247 | 0.1495 | 0.1732 | 0.2171 | 0.2563 | 0.3692 | 0.4605 |

**Table D.** Function $\ln[H_c^{(el)}(\theta, \varepsilon_{pn})]$ for various $\theta$ and $\varepsilon_{pn}$.

| $\theta$ | $\varepsilon_{pn} = \varepsilon_p/\varepsilon_n$ | | | | | | | | |
|---|---|---|---|---|---|---|---|---|---|
| | 0.125 | 0.250 | 0.500 | 0.750 | 1.00 | 1.50 | 2.00 | 4.00 | 8.00 |
| 5 | –4.235 | –4.437 | –4.787 | –5.086 | –5.345 | –5.781 | –6.138 | –7.146 | –8.312 |
| 10 | –4.209 | –4.402 | –4.738 | –5.027 | –5.279 | –5.703 | –6.054 | –7.046 | –8.202 |
| 15 | –4.176 | –4.360 | –4.683 | –4.961 | –5.206 | –5.619 | –5.962 | –6.939 | –8.085 |
| 20 | –4.136 | –4.311 | –4.621 | –4.889 | –5.126 | –5.529 | –5.864 | –6.826 | –7.960 |
| 25 | –4.089 | –4.256 | –4.553 | –4.811 | –5.040 | –5.432 | –5.760 | –6.704 | –7.827 |
| 30 | –4.035 | –4.193 | –4.477 | –4.726 | –4.947 | –5.328 | –5.647 | –6.575 | –7.686 |
| 35 | –3.973 | –4.124 | –4.395 | –4.634 | –4.848 | –5.217 | –5.528 | –6.439 | –7.537 |
| 40 | –3.904 | –4.047 | –4.306 | –4.535 | –4.741 | –5.098 | –5.401 | –6.294 | –7.378 |
| 45 | –3.828 | –3.963 | –4.210 | –4.429 | –4.627 | –4.973 | –5.267 | –6.141 | –7.211 |
| 50 | –3.743 | –3.872 | –4.106 | –4.316 | –4.506 | –4.839 | –5.125 | –5.979 | –7.035 |
| 55 | –3.651 | –3.772 | –3.994 | –4.195 | –4.377 | –4.698 | –4.975 | –5.808 | –6.848 |
| 60 | –3.550 | –3.664 | –3.875 | –4.065 | –4.240 | –4.548 | –4.816 | –5.628 | –6.651 |
| 65 | –3.441 | –3.548 | –3.747 | –3.928 | –4.094 | –4.390 | –4.648 | –5.438 | –6.443 |
| 70 | –3.322 | –3.423 | –3.610 | –3.782 | –3.940 | –4.223 | –4.471 | –5.238 | –6.224 |
| 75 | –3.194 | –3.288 | –3.464 | –3.626 | –3.776 | –4.046 | –4.284 | –5.027 | –5.993 |
| 80 | –3.056 | –3.144 | –3.308 | –3.461 | –3.602 | –3.859 | –4.087 | –4.804 | –5.749 |
| 85 | –2.908 | –2.989 | –3.142 | –3.285 | –3.418 | –3.661 | –3.878 | –4.569 | –5.491 |
| 90 | –2.748 | –2.823 | –2.965 | –3.098 | –3.223 | –3.452 | –3.658 | –4.321 | –5.218 |
| 95 | –2.576 | –2.645 | –2.776 | –2.899 | –3.016 | –3.231 | –3.426 | –4.059 | –4.929 |
| 100 | –2.391 | –2.454 | –2.574 | –2.687 | –2.795 | –2.996 | –3.179 | –3.782 | –4.623 |
| 105 | –2.192 | –2.249 | –2.358 | –2.462 | –2.561 | –2.747 | –2.918 | –3.488 | –4.298 |
| 110 | –1.977 | –2.028 | –2.126 | –2.221 | –2.311 | –2.482 | –2.641 | –3.177 | –3.952 |
| 115 | –1.745 | –1.790 | –1.878 | –1.962 | –2.044 | –2.200 | –2.345 | –2.845 | –3.584 |
| 120 | –1.494 | –1.533 | –1.610 | –1.685 | –1.758 | –1.898 | –2.030 | –2.491 | –3.189 |
| 125 | –1.221 | –1.255 | –1.320 | –1.385 | –1.449 | –1.573 | –1.691 | –2.112 | –2.766 |
| 130 | –0.9232 | –0.9508 | –1.006 | –1.061 | –1.116 | –1.223 | –1.327 | –1.705 | –2.310 |
| 135 | –0.5959 | –0.6178 | –0.6623 | –0.7074 | –0.7527 | –0.8429 | –0.9318 | –1.264 | –1.815 |
| 140 | –0.2335 | –0.2497 | –0.2835 | –0.3185 | –0.3543 | –0.4271 | –0.5004 | –0.7840 | –1.276 |
| 145 | 0.1719 | 0.1613 | 0.1383 | 0.1135 | 0.0875 | 0.0326 | –0.0245 | –0.2560 | –0.6813 |
| 150 | 0.6319 | 0.6269 | 0.6148 | 0.6004 | 0.5842 | 0.5478 | 0.5078 | 0.3319 | –0.0191 |
| 155 | 1.164 | 1.165 | 1.164 | 1.160 | 1.154 | 1.137 | 1.115 | 0.9985 | 0.7312 |
| 160 | 1.799 | 1.805 | 1.815 | 1.822 | 1.827 | 1.829 | 1.826 | 1.775 | 1.602 |
| 165 | 2.590 | 2.602 | 2.624 | 2.642 | 2.658 | 2.681 | 2.698 | 2.717 | 2.654 |
| 170 | 3.661 | 3.680 | 3.713 | 3.743 | 3.770 | 3.816 | 3.854 | 3.953 | 4.017 |
| 175 | 5.399 | 5.424 | 5.470 | 5.513 | 5.553 | 5.624 | 5.687 | 5.877 | 6.099 |

**Table E.** Function $\ln[Q(\theta,\varepsilon_{pn})]$ for various $\theta$ and $\varepsilon_{pn}$; see eq S4 below.

| | $\varepsilon_{pn} = \varepsilon_p/\varepsilon_n$ | | | | | | | | |
|---|---|---|---|---|---|---|---|---|---|
| $\theta$ | 0.125 | 0.250 | 0.500 | 0.750 | 1.00 | 1.50 | 2.00 | 4.00 | 8.00 |
| 5 | 1.816 | 1.816 | 1.817 | 1.817 | 1.817 | 1.817 | 1.818 | 1.818 | 1.818 |
| 10 | 1.776 | 1.776 | 1.777 | 1.778 | 1.779 | 1.779 | 1.780 | 1.781 | 1.781 |
| 15 | 1.734 | 1.735 | 1.736 | 1.737 | 1.737 | 1.739 | 1.740 | 1.741 | 1.742 |
| 20 | 1.690 | 1.691 | 1.693 | 1.694 | 1.695 | 1.697 | 1.697 | 1.699 | 1.701 |
| 25 | 1.643 | 1.645 | 1.646 | 1.648 | 1.649 | 1.651 | 1.653 | 1.655 | 1.657 |
| 30 | 1.594 | 1.596 | 1.599 | 1.600 | 1.602 | 1.604 | 1.605 | 1.609 | 1.611 |
| 35 | 1.542 | 1.544 | 1.548 | 1.549 | 1.552 | 1.554 | 1.557 | 1.560 | 1.562 |
| 40 | 1.487 | 1.489 | 1.493 | 1.497 | 1.498 | 1.501 | 1.503 | 1.508 | 1.511 |
| 45 | 1.429 | 1.432 | 1.436 | 1.439 | 1.442 | 1.445 | 1.448 | 1.453 | 1.457 |
| 50 | 1.367 | 1.370 | 1.375 | 1.379 | 1.381 | 1.385 | 1.388 | 1.395 | 1.400 |
| 55 | 1.301 | 1.305 | 1.310 | 1.314 | 1.318 | 1.323 | 1.326 | 1.334 | 1.339 |
| 60 | 1.231 | 1.234 | 1.241 | 1.245 | 1.250 | 1.255 | 1.260 | 1.269 | 1.275 |
| 65 | 1.155 | 1.160 | 1.167 | 1.172 | 1.177 | 1.183 | 1.188 | 1.198 | 1.206 |
| 70 | 1.075 | 1.080 | 1.088 | 1.094 | 1.099 | 1.107 | 1.112 | 1.124 | 1.134 |
| 75 | 0.9882 | 0.9939 | 1.003 | 1.010 | 1.016 | 1.024 | 1.031 | 1.045 | 1.056 |
| 80 | 0.8952 | 0.9015 | 0.9115 | 0.9194 | 0.9260 | 0.9360 | 0.9436 | 0.9598 | 0.9734 |
| 85 | 0.7948 | 0.8016 | 0.8127 | 0.8220 | 0.8295 | 0.8411 | 0.8499 | 0.8693 | 0.8844 |
| 90 | 0.6860 | 0.6936 | 0.7062 | 0.7168 | 0.7251 | 0.7385 | 0.7485 | 0.7713 | 0.7888 |
| 95 | 0.5676 | 0.5761 | 0.5905 | 0.6023 | 0.6121 | 0.6274 | 0.6391 | 0.6654 | 0.6870 |
| 100 | 0.4386 | 0.4482 | 0.4644 | 0.4779 | 0.4890 | 0.5067 | 0.5199 | 0.5510 | 0.5757 |
| 105 | 0.2976 | 0.3081 | 0.3269 | 0.3415 | 0.3543 | 0.3747 | 0.3900 | 0.4264 | 0.4561 |
| 110 | 0.1425 | 0.1534 | 0.1747 | 0.1924 | 0.2064 | 0.2294 | 0.2476 | 0.2902 | 0.3253 |
| 115 | –0.0293 | –0.0167 | 0.0069 | 0.0263 | 0.0428 | 0.0699 | 0.0913 | 0.1405 | 0.1821 |
| 120 | –0.2207 | –0.2060 | –0.1791 | –0.1576 | –0.1382 | –0.1082 | –0.0839 | –0.0258 | 0.0245 |
| 125 | –0.4352 | –0.4181 | –0.3884 | –0.3638 | –0.3416 | –0.3061 | –0.2788 | –0.2098 | –0.1512 |
| 130 | –0.6766 | –0.6578 | –0.6243 | –0.5960 | –0.5715 | –0.5309 | –0.4988 | –0.4180 | –0.3470 |
| 135 | –0.9526 | –0.9313 | –0.8939 | –0.8613 | –0.8335 | –0.7866 | –0.7497 | –0.6551 | –0.5691 |
| 140 | –1.271 | –1.247 | –1.205 | –1.168 | –1.136 | –1.083 | –1.039 | –0.9277 | –0.8244 |
| 145 | –1.644 | –1.617 | –1.570 | –1.528 | –1.491 | –1.430 | –1.379 | –1.247 | –1.122 |
| 150 | –2.089 | –2.059 | –2.006 | –1.959 | –1.916 | –1.845 | –1.787 | –1.630 | –1.478 |
| 155 | –2.633 | –2.600 | –2.539 | –2.486 | –2.438 | –2.356 | –2.289 | –2.102 | –1.914 |
| 160 | –3.324 | –3.287 | –3.219 | –3.158 | –3.103 | –3.008 | –2.929 | –2.706 | –2.472 |
| 165 | –4.249 | –4.207 | –4.130 | –4.061 | –3.998 | –3.888 | –3.795 | –3.526 | –3.231 |
| 170 | –5.602 | –5.555 | –5.469 | –5.390 | –5.318 | –5.190 | –5.080 | –4.753 | –4.373 |
| 175 | –8.016 | –7.963 | –7.864 | –7.774 | –7.691 | –7.541 | –7.408 | –7.002 | –6.498 |

## Second Procedure for Processing Meniscus-Profile Data

For contact angles $5° \le \theta \le 120°$, one can use a procedure, which is simpler than that the procedure described in section 7.2 of the main paper. Step (1) is the same as in section 7.2. In Figure 10 of the main paper, one sees that the data for $z_i^{(el)}$ vs. $y \equiv (r_c/r_i)^4$ comply with a straight line, except the points for the greatest $y$. This linear fraction of the plot corresponds to the long-distance asymptotics, described by eq 5.24. The respective data points (for not too

large $y$) can be fitted by a linear regression (the dashed line in Figure 10), whose slope and intercept can be accurately determined. For the considered illustrative example (Figure 10), we have

$$z^{(\mathrm{el})} = 14.532 - 13.596\,y \tag{S1}$$

On the other hand, because $z^{(\mathrm{el})} = h_{\mathrm{c}}^{(\mathrm{el})} + \zeta^{(\mathrm{el})}$, with the help of eq 5.24 we obtain

$$z^{(\mathrm{el})}(r) = h_{\mathrm{c}}^{(\mathrm{el})} - \frac{\pi\sigma_{\mathrm{pn}}^2 r_{\mathrm{c}}^2}{\varepsilon_{\mathrm{n}}\gamma}\frac{D^2}{8}\,y \tag{S2}$$

Thus, the ratio of the intercept and the slope is:

$$Q \equiv \frac{8\varepsilon_{\mathrm{n}}\gamma\, h_{\mathrm{c}}^{(\mathrm{el})}}{\pi\sigma_{\mathrm{pn}}^2 r_{\mathrm{c}}^2 D^2} \tag{S3}$$

In view of eq S1, the ratio of the intercept and the slope is $Q$ = 1.069 for the data in Figure 10. On the other hand, the substitution of $h_{\mathrm{c}}^{(\mathrm{el})}$ from eq 6.3 into eq S3 yields:

$$Q = \frac{16H_{\mathrm{c}}^{(\mathrm{el})}(\theta,\varepsilon_{\mathrm{pn}})}{[D(\theta,\varepsilon_{\mathrm{pn}})]^2} \tag{S4}$$

The dependence $H_{\mathrm{c}}^{(\mathrm{el})}(\theta,\varepsilon_{\mathrm{pn}})$ is given in Table D, while the dependence $D(\theta,\varepsilon_{\mathrm{pn}})$ is tabulated in ref 43. Combining the two tabulated dependencies, in Table E we have given the dependence $Q(\theta,\varepsilon_{\mathrm{pn}})$. From this table, with $\varepsilon_{\mathrm{pn}}$ = 1.946 and $Q$ = 1.069 we determine $\theta = \theta^{(\mathrm{e})}$ = 116.8° by linear interpolation. The latter value is close to $\theta^{(\mathrm{e})}$ = 117.3° determined in section 7.2.

For $\theta > 120°$, the error of the intercept of the linear regression (see eq S1) becomes too large, and its slope does not correspond to the asymptotic slope at $y \to 0$ (eq S2). For this reason, the procedure described in the present section is applicable only for $\theta \le 120°$. If the latter relation is not satisfied, one could use the procedure in section 7.2, which is applicable for every $\theta$.